



Publication Year	2016
Acceptance in OA @INAF	2020-06-19T15:26:23Z
Title	Lithologic variation within bright material on Vesta revealed by linear spectral unmixing
Authors	Blewett, D. T.; Ammannito, E.; Russell, C. T.; Raymond, C. A.; ZAMBON, Francesca; et al.
DOI	10.1016/j.icarus.2016.01.009
Handle	http://hdl.handle.net/20.500.12386/26158
Journal	ICARUS
Number	272

Accepted Manuscript

Lithologic variation within bright material on Vesta revealed by linear spectral unmixing

F. Zambon, F. Tosi, C. Carli, M.C. De Sanctis, D.T. Blewett, E. Palomba, A. Longobardo, A. Frigeri, E. Ammannito, C.T. Russell, C.A. Raymond

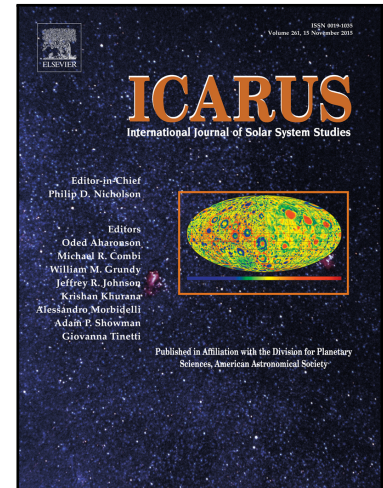
PII: S0019-1035(16)00013-0
DOI: [10.1016/j.icarus.2016.01.009](https://doi.org/10.1016/j.icarus.2016.01.009)
Reference: YICAR 11888

To appear in: *Icarus*

Received date: 26 March 2015
Revised date: 18 December 2015
Accepted date: 8 January 2016

Please cite this article as: F. Zambon, F. Tosi, C. Carli, M.C. De Sanctis, D.T. Blewett, E. Palomba, A. Longobardo, A. Frigeri, E. Ammannito, C.T. Russell, C.A. Raymond, Lithologic variation within bright material on Vesta revealed by linear spectral unmixing, *Icarus* (2016), doi: [10.1016/j.icarus.2016.01.009](https://doi.org/10.1016/j.icarus.2016.01.009)

This is a PDF file of an unedited manuscript that has been accepted for publication. As a service to our customers we are providing this early version of the manuscript. The manuscript will undergo copyediting, typesetting, and review of the resulting proof before it is published in its final form. Please note that during the production process errors may be discovered which could affect the content, and all legal disclaimers that apply to the journal pertain.



1 Lithologic variation within bright material on Vesta
 2 revealed by linear spectral unmixing

3 F. Zambon^a, F. Tosi^a, C. Carli^a, M. C. De Sanctis^a, D. T. Blewett^b, E.
 4 Palomba^a, A. Longobardo^a, A. Frigeri^a, E. Ammannito^c, C. T. Russell^c and
 5 C. A. Raymond^d

6 ^a*INAF-IAPS Istituto di Astrofisica e Planetologia Spaziali, Via del Fosso del Cavaliere,*
 7 *100, 00133 Rome, Italy;*

8 ^b*Johns Hopkins University Applied Physics Laboratory, Laurel, Maryland, USA;*

9 ^c*Institute of Geophysics and Planetary Physics, University of California at Los Angeles,*
 10 *3845 Slichter Hall, 603 Charles E. Young Drive, East, Los Angeles, CA 90095-1567,*
 11 *USA;*

12 ^d*NASA/Jet Propulsion Laboratory and California Institute of Technology, 4800 Oak*
 13 *Grove Drive, Pasadena, CA*

14 * Corresponding author: Francesca Zambon
 15 INAF-IAPS Istituto di Astrofisica e Planetologia Spaziali
 16 Via del Fosso del Cavaliere, 100, 00133 Rome, Italy
 17 Phone: +39-06-45488210
 18 Fax: +39-06-45488188
 19 Email: francesca.zambon@iaps.inaf.it

20 **Submitted to: Icarus**
 21

22 **Abstract**

23 Vesta's surface is mostly composed of pyroxene-rich lithologies compatible
 24 with howardite, eucrite and diogenite (HED) meteorites (e.g., McCord et al.,
 25 1970; Feierberg and Drake, 1980). Data provided by the Visible and Infrared
 26 (VIR) spectrometer, onboard the NASA Dawn spacecraft, revealed that all
 27 Vesta reflectance spectra show absorption bands at $\sim 0.9 \mu\text{m}$ and $\sim 1.9 \mu\text{m}$,

28 which are typical of iron-bearing pyroxenes (De Sanctis et al., 2012a). Other
29 minerals may be present in spectrally significant concentrations; these in-
30 clude olivine and opaque phases like those found in carbonaceous chondrites.
31 These additional components modify the dominant pyroxene absorptions.
32 We apply linear spectral unmixing on bright material (BM) units of Vesta to
33 identify HEDs and non-HED phases. We explore the limits of applicability
34 of linear spectral unmixing, testing it on laboratory mixtures. We find that
35 the linear method is applicable at the VIR pixel resolution and it is useful
36 when the surface is composed of pyroxene-rich lithologies containing moder-
37 ate quantities of carbonaceous chondrite, olivine, and plagioclase. We found
38 three main groups of BM units: eucrite-rich, diogenite-rich, and olivine-rich.
39 For the non-HED spectral endmember, we choose either olivine or a fea-
40 tureless component. Our work confirms that Vesta's surface contains a high
41 content of pyroxenes mixed with a lower concentration of other phases. In
42 many cases, the non-HED endmember that gives the best fit is the featureless
43 phase, which causes a reduction in the strength of both bands. The anticor-
44 relation between albedo and featureless endmember indicates that this phase
45 is associated with low-albedo, CC-like opaque material. Large amounts of
46 olivine have been detected in Bellicia, Arruntia and BU14 BM units. Other
47 sites present low olivine content ($< 30\%$) mostly with a high concentration
48 of diogenite.

49 HIGHLIGHTS

- 50 • Characterization of Vesta's bright material (BM) units by linear un-
51 mixing analysis;

- 52 • Detection of different lithologies within BM regions;
- 53 • Detection of phases other than pyroxenes from VIR data on Vesta
54 surface;
- 55 • Calculation of mixing coefficients for the detected lithologies for each
56 in BM unit;

57 **1. Introduction**

58 *1.1. Early knowledge of Vesta*

59 The first spectral study of Vesta dates back to Bobrovnikoff (1929). Mc-
60 Cord et al. (1970) compared Vesta spectra with the meteorite Nuevo Laredo,
61 inferring a relation between Vesta and pyroxenes. Pyroxenes are character-
62 ized by the presence of two crystal field absorptions, centered approximately
63 at 0.9 and 1.9 μm (McCord et al., 1970), due to ferrous iron (Fe^{+2}) in octa-
64 hedral sites (e.g., Burns, 1993). Consolmagno and Drake (1977) suggested a
65 possible link between Vesta and eucrite meteorites, and Feierberg and Drake
66 (1980) proposed that Vesta is a mixture of howardite and eucrite. Studies by
67 Lupishko et al. (1988) show a clear inverse correlation between the polariza-
68 tion and brightness of Vesta, correlated with the west-east dichotomy. Hubble
69 Space Telescope (HST) observations between 1994 and 1996 confirmed this
70 inference by highlighting the geological differences on the asteroid (Binzel
71 et al., 1997). Moreover the identification of the prominent impact basin
72 at the south pole (now named Rheasilvia) corroborates the hypothesis that
73 Vesta is the parent body of the howardite, eucrite and diogenite (HED) me-
74 teorites (Thomas et al., 1997). In addition, the disk-integrated mid-infrared

75 spectra of Vesta have shown the presence of minor constituents as olivine,
76 feldspar, and chromite (Donaldson Hanna and Sprague, 2009). Studies by Li
77 et al. (2010) revealed that the vestan surface can be divided into several geo-
78 logical units (more specifically, regions of lithologic variation), in particular,
79 eucrite-rich and diogenite-rich units, as well as slightly weathered and freshly
80 exposed units. Shestopalov et al. (2010) concluded that the global diversity
81 of Vesta might be caused by variations of non-basaltic source sediments en-
82 riched by dark rocks, spinel group minerals, or even chondritic-like material.
83 Moreover, they showed that certain vestan units contain olivine abundances
84 of several volume percent.

85 *1.2. The Dawn-Era and Vesta's lithologies*

86 Dawn entered orbit around Vesta in July 2011 (Russell and Raymond,
87 2011), and enabled many discoveries during about one year of observations.
88 For the first time, Dawn acquired data of Vesta's surface at high spatial res-
89 olution, allowing for production of complete geological and lithological maps
90 (De Sanctis et al., 2012a; Williams et al., 2014). Dawn's Visible and Infrared
91 (VIR) imaging spectrometer (De Sanctis et al., 2011) provided high spectral
92 resolution data covering the majority of Vesta's surface at varying spatial
93 scales. The spatial resolution of the VIR maps ranges from ~ 800 m/pixel in
94 the Survey phase to ~ 180 m/pixel in the HAMO and HAMO-2 phases (see
95 Table 1 of Zambon et al. (2015)).

96 Vesta is the parent body of the HED meteorites. HEDs encompass a large va-
97 riety of igneous rocks, similar to basalts, cumulate gabbros, orthopyroxenites
98 and igneous brecciated mixtures (Mittlefehldt et al., 1998). The diogenites
99 are coarse-grained cumulates that originated in a plutonic layer deep in the

100 crust (Mittlefehldt et al., 1998; Beck and McSween, 2010; McSween et al.,
101 2011, 2013). The mineralogy of diogenites is dominated by orthopyroxenes
102 (from 87% to 99%); all diogenites contain < 5% chromite and some contain
103 olivine, typically at contents < 10% (McSween et al., 2011). Eucrites occur
104 as basaltic or cumulate rocks. They are dominated by Ca-poor pyroxenes
105 and plagioclase, with minor amounts of metal, troilite, chromite, ilmenite,
106 and silica (Mayne et al., 2010; McSween et al., 2011). Eucrites are believed
107 to have crystallized as lavas on the surface or within relatively shallow dikes
108 and plutons (McSween et al., 2011). Basaltic eucrites contain Fe-rich pyrox-
109 enes, whereas cumulate eucrites are predominantly unbrecciated and their
110 chemistry is similar to basaltic eucrites, but richer in Mg (Mittlefehldt et al.,
111 1998; McSween et al., 2011). Howardites are brecciated achondrites, prin-
112 cipally mixtures of eucrite and diogenite clasts, and reflectance spectra of
113 howardites have pyroxene band center positions intermediate between those
114 of eucrites and diogenites (Mittlefehldt et al., 1998; McSween et al., 2011).
115 Impact mixing of eucrite and diogenite has produced the polymict breccias
116 and howardites.

117 Eucrite, diogenite and howardite lithologies are present on Vesta's surface,
118 as revealed by VIR data (De Sanctis et al., 2012a; Ammannito et al., 2013a)
119 augmented by Dawn Framing Camera images (Reddy et al., 2012b) and
120 Gamma Ray And Neutron Detector data (Lawrence et al., 2013; Prettyman
121 et al., 2011, 2013, 2014). Recently, many papers on the analysis of Vesta's
122 surface composition using Dawn data have been published (e.g., Ruesch et al.
123 (2014); Ammannito et al. (2013a); De Sanctis et al. (2013b); Le Corre et al.
124 (2013); Reddy et al. (2013); Thangjam et al. (2013)). The crust of Vesta is

125 dominated by howardite enriched in eucrite (De Sanctis et al., 2012a, 2013b).
126 A few outcrops of diogenite are present in localized areas in the south po-
127 lar region, corresponding to the rim of the large impact basin Rheasilvia.
128 Large areas of diogenite-enriched howardite have also been identified in the
129 northern hemisphere (longitude 0° - 90°E) and are interpreted to consist of
130 Rheasilvia ejecta (De Sanctis et al., 2012a; Ammannito et al., 2013a).
131 Ammannito et al. (2013a) suggested a high content of olivine (50-80 vol.%)
132 in the area of Bellicia (lat 40°N , lon 40°E) and Arruntia craters (lat 40°N , lon
133 70°E), highlighting the presence of lithologies different from that of typical
134 HEDs. Others eleven sites containing much smaller amounts of olivine (lo-
135 cated up to 39°S latitude) have also been identified by Ruesch et al. (2014),
136 and six other new olivine-rich regions were proposed by Palomba et al. (2015),
137 almost all located at latitudes below 28°N . Dark material units on Vesta
138 were discussed by Jaumann et al. (2012); McCord et al. (2012); Reddy et al.
139 (2012a), and Palomba et al. (2014). Hydrated mineral phases were shown to
140 be correlated with this low-reflectance material (De Sanctis et al., 2012b),
141 confirming that the dark material can be attributed to the presence of a
142 carbonaceous chondrite (CC)-like component delivered by impacts.

143 *1.3. Bright material units: A slice of fresh material*

144 The spectral analysis of the bright material units reveals that they are
145 generally characterized by greater band depths than their surroundings. Most
146 bright units have a howardite rich-eucrite, composition, with some exceptions
147 such as the bright unit called "BU15" in Zambon et al. (2014).

148 BM units could represent pristine material that has been recently exposed
149 on the surface, and thus contains less carbonaceous-chondrite-like contami-

150 nation introduced by impact mixing than other areas of Vesta (see Zambon
151 et al. (2014) for more detail). To be consistent with Zambon et al. (2014), we
152 follow the same classification of the BM units, as described by Mittlefehldt
153 et al. (2012). The abbreviation CWM stands for crater wall material, SM
154 means slope material, and RM refers to radial material. The spectral anal-
155 ysis employed in Zambon et al. (2014) to derive Vesta's lithologies is based
156 on selected spectral parameters, namely band center (BC), band depth (BD)
157 and Band Area Ratio (BAR).

158 The goal of our work is to use linear spectral unmixing to automatically
159 identify the main lithologies of specific regions and determine their semi-
160 quantitative mixing coefficients, including identification and mapping of min-
161 eralogical phases other than the spectrally dominant pyroxenes. The mixing
162 coefficients depend on various effects, such as, the grain size, the abundance
163 of the mineralogical phases present in the scene, and the scale at which the
164 components are mixed (i.e., macroscopic vs. intimate; Combe et al. (2008)).
165 Since the grain size on Vesta, at the VIR spatial scale, is quite homogeneous
166 ($< 25 - 45 \mu\text{m}$) (Hiroi et al., 1994; Palomba et al., 2014; Zambon et al.,
167 2014), we can assume that the grain size does not substantially affect our
168 derived mixing coefficients. Thus the unmixing results principally depend on
169 the abundance of the mineralogical phases and on the type of mixing.

170 Unmixing methods are useful for understanding the composition of a surface
171 (e.g. Pieters and Englert, 1993; Keshava and Mustard, 2002; Bioucas-Dias
172 et al., 2012). Mixing models can be either linear or non-linear. In the linear
173 case, the spectrum of a region can be considered the area-weighted average of
174 the endmembers present (Singer and McCord, 1979; Hapke, 1993; Bioucas-

175 Dias et al., 2012). The endmembers can be extracted from the scene, or
176 can be reference spectra of plausible analogue phases. The endmembers are
177 generally assumed to represent the different components, which are the fun-
178 damental constituents of the scene, so that each pixel in the scene can be
179 modeled as a linear combination of the endmembers (Bioucas-Dias et al.,
180 2012).

181 The case of non-linear mixing arises when light is scattered by multiple mate-
182 rials in the scene. Scattered light interacts with more than one endmember,
183 and the resulting spectrum is a non-linear combination of the components.
184 Models for non-linear mixing require comprehensive information on the ex-
185 pected minerals, such as scattering coefficients, particle sizes, and optical
186 constants (e.g., Hapke (1981); Shkuratov et al. (1999)). Here we use linear
187 unmixing as a first step in order to derive additional information on the com-
188 position of Vesta's surface.

189 Many authors have linear unmixing algorithms for analysis of remote sensing
190 data for a variety of bodies (e.g., Adams et al. (1986); Fox III et al. (1990);
191 Ramsey and Christensen (1992); Blewett et al. (1995); Combe et al. (2008);
192 Dalton (2007); McCord et al. (2012)). Adams et al. (1986) already applied
193 linear unmixing methods to Viking lander data of Mars, while Dalton (2007)
194 applied linear unmixing to Europa data using a set of laboratory spectra as
195 endmembers, and Combe et al. (2008) used the Multiple-Endmember Lin-
196 ear Spectral Unmixing Model (MELSUM) to analyze Mars data from the
197 Infrared Mineralogical Mapping Spectrometer (OMEGA) onboard MarsEx-
198 press. A first use of linear unmixing methods on Vesta was presented by
199 McCord et al. (2012), who found that the entire surface of Vesta as observed

200 by VIR could be modeled using the weighted sum spectral endmembers,
201 'bright' and 'dark' (McCord et al., 2012). In this paper, we apply the same
202 linear unmixing method employed by Tosi et al. (2015) and Zambon et al.
203 (2015) to extended areas of Vesta.

204 Here we considered high spatial resolution data from the Dawn mission at
205 Vesta, and we selected a set of plausible laboratory spectra analogues as
206 endmembers. We apply the linear unmixing method to the bright material
207 (BM) units of Vesta, previously analyzed by Zambon et al. (2014). BM units
208 are often associated with impact craters. Impacts expose fresh, unweathered
209 material from beneath the surface, which could be indicative of the original
210 vestan crust composition (Zambon et al., 2014). The previous spectral anal-
211 ysis revealed the main lithologies (eucrite, diogenite and howardite) and the
212 spectral characteristics of these units. Here we study the same BM units with
213 the goal of quantifying the mixing coefficients of the different lithologies. We
214 also aim to identify the presence of other mineralogical phases in addition to
215 the spectrally dominant, HED components. In principle, this work can be
216 extended also to larger region on Vesta, determining the global distribution
217 of Vesta's non-HED lithologies.

218 **2. Dataset description and VIR spectra characteristics**

219 The Dawn mission at Vesta consisted of four phases, based on the alti-
220 tude of the spacecraft: Survey (2735 km altitude), HAMO (High Altitude
221 Mapping Orbit, 695 km), LAMO (Low Altitude Mapping Orbit, 210 km)
222 and HAMO-2, an extension of the mission similar to the HAMO phase (Rus-
223 sell and Raymond, 2011). Here we used HAMO and HAMO-2 VIR data,

224 which cover large part of Vesta's surface with a high spatial resolution (~ 180
225 m/pixel). The VIR instrument has two distinct detectors, or "channels": the
226 visible, covering wavelengths from $0.25 \mu\text{m}$ to $1.07 \mu\text{m}$, and the infrared, with
227 sensitivity from $1.02 \mu\text{m}$ to $5.10 \mu\text{m}$ (De Sanctis et al., 2011). Each channel
228 has 432 spectral bands, so the average spectral sampling is 1.8 nm/band for
229 the visible channel and 9.8 nm/band for the infrared channel (De Sanctis
230 et al., 2011). Each VIR image cube has 256 spatial samples with a variable
231 number of lines determined by the length of a scan, and 432 spectral bands.
232 For details about the VIR data calibration, refer to a document archived
233 at the NASA Planetary Data System Small Bodies Node: http://sbn.psi.edu/archive/dawn/vir/DWNVVIR_I1B/DOCUMENT/VIR_CALIBRATION/VIR_CALIBRATION_V2_4.PDF.
234 The VIR visible and infrared data are each separately geo-
235 referenced, then the two VIS and IR subsets are merged together to form
236 a single spectrum covering the entire spectral range from 0.25 to $5.10 \mu\text{m}$.
237 The last 19 spectral channels of the visible range, which usually are affected
238 by higher instrumental noise, are discarded.

240 In this work described here, we consider VIR data calibrated in units of re-
241 flectance factor (I/F) from $0.6 \mu\text{m}$ to $2.5 \mu\text{m}$, focusing our analysis on the
242 two pyroxene bands. We considered the average spectra of BM units used for
243 spectral characterization by Zambon et al. (2014). The wavelength position
244 of the centers of the two bands gives information on the HED lithologies.
245 The displacement of the pyroxene band centers is sensitive to temperature
246 variations (e.g., Burbine et al. (2009), Reddy et al. (2012c)). However, given
247 the usual range of daytime temperatures recorded on Vesta for BM units (be-
248 tween 252 and 265 K , Tosi et al. (2014)), this effect is essentially negligible

249 in VIR data (Longobardo et al., 2014).

250 The strength (depth) of the pyroxene absorption bands is a function of the
251 abundances of the minerals, the particle size, and the presence of opaque
252 phases (e.g., Clark (1999)). Band depths are also affected by temperature
253 variations and the phase angle of the observations (Longobardo et al., 2014;
254 Reddy et al., 2012c). The relatively small range of temperatures found on
255 Vesta does not affect the band depth shape: Dalton et al. (2011) demon-
256 strated that a temperature range of 150K is necessary to observe substantial
257 band-depth effects (whereas on Vesta we found variations never larger than
258 50 K). Band depths are the only spectral parameter among those considered
259 that vary depending on illumination and viewing geometry. However, the
260 variation of band depth with phase angle is very small for bright regions,
261 although variation can become important as albedo decreases (Longobardo
262 et al., 2014). In this work, observations at phase angles between 28° and
263 52° and incidence angles lower than 60° have been selected. According to
264 Longobardo et al. (2014), in this narrow range band depths are only weakly
265 dependent on phase and hence a photometric correction is not mandatory.
266 Phase, incidence and emission angles of the BM units are reported in Tables
267 7, 8 and 9 of the Zambon et al. (2014) supplementary online material (SOM).
268 In this work, we utilize the "Claudia" coordinate system (supplemental ma-
269 terial of Russell et al., 2012; Li et al., 2012; Roatsch et al., 2012; Reddy et al.,
270 2013), which has been used by Zambon et al. (2014) for tabulation of the
271 BM unit locations.

272 3. Analytical method

273 3.1. Linear unmixing

274 Understanding the composition of a surface using reflectance spectroscopy
 275 may be challenging. Analysis of spectral parameters is useful but does not offer
 276 a complete characterization of the surface materials. Key additional information
 277 can be provided by the application of mixing model algorithms. Based
 278 on past analysis (De Sanctis et al., 2012a; Jaumann et al., 2012; McCord
 279 et al., 2012; Ammannito et al., 2013a; De Sanctis et al., 2013a), we assume
 280 that reflectance spectra of Vesta can be reproduced by a linear combination
 281 of at least three endmembers, chosen from a sample of eucrites, diogenites,
 282 olivines and a featureless endmember. To describe the primary components
 283 of Vesta’s surface, we consider only diogenite and eucrite endmembers, and do
 284 not include howardite as a separate endmember. Howardites, which are the
 285 major component of Vesta terrains (De Sanctis et al., 2012a), are brecciated
 286 rocks with variable amounts of both eucrite and diogenite; thus howardites
 287 can be spectrally characterized by a mixing of the two components. The
 288 mixing equation is:

$$Y_{mix} = a_1y_1 + a_2y_2 + a_3y_3 \quad (1)$$

289 where y_1, y_2, y_3 are the scaled spectra of the endmembers and a_1, a_2, a_3 are
 290 their respective mixing coefficients. The unmixing algorithm requires all
 291 mixing coefficients to be non-negative, and their sum must be equal to unity.

292 The method we developed is able to automatically find the endmembers
 293 and the mixing coefficients, subject to the positivity constraint, which allows
 294 exclusion of solutions that are not physically meaningful. We outline the
 295 principal steps of our algorithm as follows:

296 1. Spectral slope removal. Normalization of the spectrum by the contin-
 297 uum slope is done for two reasons. First, the position of the band center
 298 is defined as the location of the reflectance minimum inside the band
 299 as measured on a continuum-removed spectrum. Second, the process
 300 of continuum normalization removes the influence of albedo from the
 301 unmixing process. Albedo is closely tied to the photometric conditions
 302 of the observation rather than mineralogy of the surface. To remove
 303 the slope, we consider the line between the first point ($0.6 \mu\text{m}$) and
 304 the last point ($2.5 \mu\text{m}$) of the spectrum, then we divide the spectrum
 305 by this line. To be consistent, the slope was removed in the same way
 306 from both VIR spectra and the spectral endmembers (See Fig. 1).

307
 308 FIGURE 1
 309

310 2. We selected a sample of 14 laboratory spectra from a larger spectral
 311 library. In Section 3.2, we describe in detail the endmembers and the
 312 criteria for their selection.

313 3. We calculate the χ^2 values for all the combinations. We select the
 314 best fit spectrum corresponding with the minimum χ^2 value, with a
 315 confidence limit of 95%. In Table 2, we report all the χ^2 values of the
 316 bright units, associated to the best-fit, with the corresponding values
 317 of the correlation coefficient (r).

318 Following these steps, the algorithm is able to determines automatically the
 319 best combination of endmembers that describe the scene, along with their
 320 mixing coefficients. We accept only best fits with $\chi^2 < 1$.

321 *3.2. Endmembers selection*

322 Careful choice of endmembers is necessary to obtain consistent results.
323 In our case, we consider as endmembers a number of laboratory spectra,
324 accounting for pure minerals and for HED meteorites that are assumed to be
325 representative of materials that may be present on Vesta's surface.

326 We select the endmembers from the Reflectance Experiment Laboratory
327 (RELAB) database (<http://www.planetary.brown.edu/relabdocs>). The
328 endmembers selection includes consideration of the particle size. The supple-
329 mentary online material from Reddy et al. (2012b) discusses the grain size
330 differences between eucrite and diogenite. Studies based on the analysis of
331 HED laboratory samples show that the grain size of diogenites in howardite
332 breccias ranges from 500 μm to 1.5 millimeters whereas the average grain size
333 of eucritic material is $\leq 70 \mu\text{m}$ (Beck et al., 2011; Reddy et al., 2012b SOM).
334 Previous work based on ground-based observation and remote sensing data
335 suggest that for the spatial resolution available, most of Vesta's surface can
336 be best represented by regolith with particle sizes $< 25\mu\text{m}$ (Hiroi et al., 1994;
337 Palomba et al., 2014; Zambon et al., 2014). This limits our choice to labo-
338 ratory spectra acquired for samples in the $< 25\mu\text{m}$ size fraction, if available.
339 Since we are working with continuum-removed spectra, absolute reflectance
340 does not enter in our analysis. Therefore, we cannot distinguish between a
341 low-reflectance featureless phase and a high-reflectance featureless phase: we
342 can just observe a decrease in band depth. To account for this effect, we
343 introduce a featureless endmember represented by a straight horizontal line.
344 Nonetheless, examination of the mean albedo values derived in Zambon et al.
345 (2014) for all the bright units can be useful in identifying the presence of low-

346 vs. high-reflectance featureless endmembers.

347 We selected 14 endmember spectra including six eucrite, five diogenite
348 and two olivine samples from the RELAB database, plus the straight line
349 representing a featureless endmember. This limit is imposed in order to
350 allow computations to be completed in reasonable time. Since eucrite-rich
351 howardite is the dominant component on Vesta's surface (De Sanctis et al.,
352 2013b) and because eucrites show a wide range of petrographic and spectral
353 characteristics, we include a larger number of them in our endmembers set.
354 The endmembers selection was done by considering the spectral parameters,
355 the spectral shape and their petrographic differences. We selected spectra
356 with band centers and band depths that cover the possible range of values
357 (Fig. 2), and those with different spectral characteristics, to take into ac-
358 count all of the possible spectral variations (see Fig. 3). Moreover for eucrite
359 we considered both cumulate and basaltic samples, as well as polymict and
360 monomict material. We also tested the distribution frequency of each spec-
361 trum from a preliminary combination of two endmembers chosen among the
362 whole available spectral library, performing a linear unmixing test. With just
363 two endmembers, the entire library of laboratory spectra can be used in the
364 analysis because of the reduced computational time. We calculate the spec-
365 tral parameters with the same methods described in Section 4 of Zambon et
366 al. (2014).

367 In Fig. 4, we show the frequency of the endmembers found in the case of
368 a linear combination of two endmembers. Eucrite appears to be the most
369 abundant component (68% of the total components), followed by diogenite
370 (25%) and olivine (7%). Taking the above discussion into consideration, we

371 select for our analysis: 1) the eucrites Bereba (6e), Bouvante (7e), Cachari
372 (8e), Padvarninkai (20e), Serra de Mage (22e), Y74450 (24e); 2) the diogen-
373 ites ALH77256 (2d), GRO95555 (5d), (6d) Johnstown, (8d) Tatahouine and
374 Y75032 (10d); and 3) two olivine samples, Jackson County (1o) and Green
375 olivine (2o) (see Table 1). In Fig. 3 we plot the selected endmembers.

376 FIGURE 2, 3, 4

377 TABLE1

378

379 4. Evaluation and limits of the linear method

380 Linear spectral unmixing can be a satisfactory approach for evaluating
381 the composition of a surface (e.g. Combe et al. (2008); Bioucas-Dias et al.
382 (2012)), even if a surface is a non-linear (intimate) mixture of several min-
383 eralogical phases. The linear assumption implies an error in the estimation
384 of the abundances, but permits only a semi-quantitative estimation of the
385 different components. In this regard, we performed two types of tests: 1)
386 We selected different laboratory mixtures of possible Vesta analogues and
387 we applied linear unmixing to the spectra of such mixtures. This exercise
388 provides an idea of the uncertainty in the determination of the abundances.
389 2) We evaluate the stability of the solution for the VIR data by considering
390 the ten cases showing smaller values of χ^2 . If for these χ^2 values we find the
391 same endmembers and similar mixing coefficients, then the solution is stable
392 and the results are reliable.

393 *4.1. Test on laboratory mixtures*

394 To perform this test, we use spectra for sets of mixtures available in the
395 RELAB database, and those used in Cloutis et al. (2013) and Serventi et al.
396 (2013). In Table 1 of the supplementary online material (SOM), we list the
397 spectral endmembers of the mixtures, indicating the origin, the particle size
398 and the texture. We selected mixtures with particle sizes similar to those
399 inferred for Vesta. In particular, we consider mixtures of two and three
400 laboratory spectra:

- 401 1. Olivine and orthopyroxene mixtures;
- 402 2. Orthopyroxene and plagioclase mixtures;
- 403 3. Millbillillie eucrite and Murchison carbonaceous chondrite;
- 404 4. Plagioclase, low and high calcium pyroxenes;
- 405 5. Olivine, low and high calcium pyroxenes;

406 In Section 1 of the SOM and in Fig. 5, all the results obtained for the
407 laboratory mixtures are displayed.

408 We notice that the error in the estimation of the mixing coefficients de-
409 pends on the number of endmembers in the mixture and on the endmember
410 itself. Generally, for mixtures of two pyroxenes with a third phase (e.g.,
411 plagioclase or olivine), we found differences between the true values and
412 the modeled mixing coefficient up to 11% for the non-pyroxene endmember.
413 In particular, for the case in which the third component is plagioclase, we
414 have an underestimation of this phase of as much as 11% if its abundance
415 is $> 50\%$. In mixtures with plagioclase contents $< 40\%$, the error is lower
416 (Table 2 and Fig. 1 of the SOM). If olivine is one of the endmembers, the

417 difference between the measured abundances and the modeled mixing coef-
418 ficients is about +10%, when the olivine abundance is $\sim 70\%$. For lower
419 proportions of olivine in the mixture, the differences between measured and
420 modeled values are decreased (Table 3 and Fig. 2 of SOM and Fig. 5).

421 For mixtures of just two minerals, the results are similar for low calcium
422 pyroxenes and olivine. The estimated error increases with greater amounts
423 of olivine. In the case of an olivine content of 90%, we found the underes-
424 timation of olivine to be 15% (Table 4 and Fig. 3 of the SOM). For lesser
425 proportions of olivine, the error is below 8%. For plagioclase mixed with
426 orthopyroxene at ratios ranging from 90:10 to 20:80, we find a consistent
427 underestimation of plagioclase from 12 to 19% (Table 5 and Fig. 4 of the
428 SOM).

429 Two-component mixtures of Murchison CC with Millbillillie eucrite have a
430 completely different trend. For Murchison abundances from 5% to 50%, the
431 mixing model consistently overestimated the CC component. The error in
432 CC abundance ranges from 11 to 26% despite the low χ^2 values (Table 6 and
433 Fig. 5 of the SOM). We consider good model results to be those for which
434 the difference between measured and modeled values is 5% (absolute) or less,
435 and we deem results to be acceptable when the difference is $< 10\%$. Cases
436 for which the difference between measured and the modeled values is over
437 10% were rejected. Our tests on laboratory mixtures reveal that some mix-
438 tures can be modeled successfully with the linear method, while some other
439 mixtures may not. Mixtures of different pyroxenes and mixture of pyroxenes
440 with olivine allow a good estimation of the mixing coefficients with the linear
441 methods with respect to the other types of mixtures. In the case of Vesta, we

442 can spectrally model its surface as a mixture of at most three endmembers:
443 pyroxenes, olivine, and a featureless component.

444 As mentioned previously, our analysis does not consider the absolute re-
445 flectance, thus we cannot distinguish high- and low-reflectance featureless
446 phases, but rather the presence of a generic featureless component that weak-
447 ens and modifies the bands. In the case of plagioclase, we find that the error
448 on plagioclase mixing coefficient decreases with increasing number of end-
449 members. Unfortunately laboratory data for mixtures of two pyroxenes with
450 CC are not available.

451

452 FIGURE 5

453

454 *4.2. Stability of the method*

455 To test the stability of the method we consider the results of the ten
456 models showing the smaller χ^2 values. The method can be considered stable
457 if, for small χ^2 variations, the results do not vary substantially. If small χ^2
458 variations lead to different endmembers, then the model results cannot be
459 considered to be reliable. In Fig. 6 we plot the best-fit spectrum for the ten
460 Aelia-SM cases with the lowest χ^2 . Variations in χ^2 of the order of 0.0001
461 led to variations of 1% in the abundances estimation, while the endmembers
462 remain unchanged, indicating robust results. We performed this test on all
463 the VIR spectra under consideration, and we obtained similar results. We
464 thus can conclude that our method yields stable solutions for the choice of
465 the endmembers and the estimation of the mixing coefficients.

466

467 FIGURE 6

468

469 **5. Bright material units: Lithological variation as revealed by lin-**
470 **ear unmixing**

471 A first statistical analysis of the BM units on Vesta indicates that the
472 algorithm always chooses three endmembers, and two of these are generally
473 eucrite and diogenite, with comparable frequency ($\sim 33\%$) (Fig. 7). The
474 third endmember is the featureless one with a frequency of 24.8%, while
475 olivine is present in few BM units with a frequency of 8.6% (Fig. 7).

476 Plots in Fig. 8 show a dependence between the modeled mixing coefficients
477 for eucrite and diogenite found here and the Zambon et al. (2014) band
478 centers for the BM units. We find that the content of eucrite increases with
479 increasing values of band centers, while the content of diogenite increases with
480 decreasing values of band centers. We observe a better correlation between
481 the band II center and eucrite and diogenite mixing coefficient, than for
482 the band I center. Generally, the band I center has a lower variability with
483 respect to the band II center (see De Sanctis et al. (2012a); Ammannito et al.
484 (2013a); Zambon et al. (2015)). The poorer correlation between the band I
485 center and the eucrite and diogenite mixing coefficients is mainly due to VIR
486 instrumental problems in the vicinity of band I, and on the bridging of the
487 visible and infrared channels. Thus we observe a better correlation between
488 mixing coefficients of eucrite and diogenite and the band II center than for
489 the band I center.

490 In Fig. 9, we show the linear unmixing application for some representative

491 case of BM units. All the results have been reported in Table 2 and in section
492 2 of the SOM.

493 Aelia is a small crater (4.34 km) located at 14.26°S 140.6°E. It is char-
494 acterized by mixed dark and bright material in its ejecta and by a high
495 diogenite content in its bright slope material (Palomba et al., 2014; Zambon
496 et al., 2014). Linear unmixing results indicate high mixing coefficient of dio-
497 genite (67%) for the Aelia-SM and only 9% of eucrite as expected. Aelia-RM
498 which represents the ejecta showing a greater amount of eucrite than diogen-
499 ite and a particularly large amount of the featureless endmember (33%). The
500 lower reflectance values of this BM unit suggest the presence of a dark phase
501 that is responsible for reducing the band depths (Fig. 9). Another diogenitic
502 unit is Licinia-SM (Zambon et al., 2014), with mixing coefficients of diogen-
503 ite (53%) higher than eucrite (30%) (Fig. 9). The bright units with shorter
504 band centers are BU5-CWM and BU5-RM (Zambon et al., 2014), for these
505 BM units we find a diogenite content of 65% and 57% respectively (Fig. 7 of
506 the SOM) and BU8-CWM with a diogenite mixing coefficient of 65% (Fig. 8
507 of the SOM). Consistent with the findings of Zambon et al. (2014), the most
508 eucritic BM units are Eumachia-CMW with an eucrite mixing coefficient of
509 57% and a corresponding diogenite content of 14% of diogenite (Fig. 9), and
510 Tuccia-RM with 57% of eucrite and 27% of diogenite (Fig. 14 of the SOM).

511 Olivine on Vesta has been identified in few areas, most notably in the
512 region of Bellicia and Arruntia craters, but smaller olivine amounts have
513 been found also near the Albana and Pomponia craters, also located in the
514 northern hemisphere (Palomba et al., 2015). Local olivine enrichments have
515 been suggested by Ruesch et al. (2014) to be present also in the equatorial

516 region and in the southern hemisphere. Our analysis suggests that olivine is
517 present in several BM units, with amounts between 12 and 53%. We identify
518 sites with large olivine mixing coefficients ($> 48\%$) in correspondence with
519 Arruntia, Bellicia in agreement with Ammannito et al. (2013b), and BU14
520 indicated as detection 3 reported by Ruesch et al. (2014). In these spectra we
521 observe a band I asymmetry typical of olivine and a reduction in the depth of
522 band II, indicating a relatively high amount of olivine, but not high enough
523 to completely obscure band II (Fig. 7). Among the possible olivine-bearing
524 sites found by Ruesch et al. (2014), we note that the Licinia-SM BM unit
525 has a mixing coefficient of olivine as high as 19%. Our algorithm chooses
526 olivine as a third endmember also for regions different from those observed
527 by Ammannito et al. (2013b) and Ruesch et al. (2014). Generally we find an
528 olivine mixing coefficient $< 30\%$ for these sites, except for Calpurnia-CWM
529 which has an olivine mixing coefficient of 35% (Fig. 10 of the SOM).

530 We cannot distinguish between opaque and neutral/featureless, high re-
531 flectance components. In Fig. 10 we show the relationship between albedo
532 of the BM units (Schröder et al., 2013) and the modeled mixing coefficient of
533 the featureless endmember. In this plot, the albedo tends to decrease with
534 increasing mixing coefficient of the featureless component. We interpret this
535 trend as an indication that the algorithm's selection of the flat endmember
536 can be attributed to the presence of an opaque dark phase in most cases.
537 However, some exceptions exist. The bright streak called BU-15 SM is the
538 brightest unit on Vesta, with a higher content of diogenite (47%) than eucrite
539 (30%). This unit is different from the others because it is characterized by
540 a reduction of the band depth with respect to the surroundings even though

541 it has high albedo (Zambon et al., 2014). The model composition of BU-15
542 SM is eucrite and diogenite, with a featureless endmember mixing coeffi-
543 cient of 23% (Table 2). Thus, BU-15 SM may represent a unique case on
544 Vesta, where the presence of a high-albedo featureless component, such as
545 plagioclase, plays an important role in controlling the spectral properties.

546 FIGURE 7, 8, 9,10

547

548 6. Discussion

549 The global compositional analyses hitherto performed on Vesta's surface
550 with Dawn/VIR data were based on the spectral parameters of the kind
551 used by De Sanctis et al. (2012a), and Ammannito et al. (2013b). Spectral
552 parameters are very useful for determining the main lithology of a surface,
553 but for a quantitative analysis mixing models are necessary.

554 In this work we focused our attention on eucrite and diogenite as the
555 dominant components, plus olivine or a featureless material. We analyzed
556 the Vesta spectra for BM units discussed by Zambon et al. (2014). In that
557 paper, the authors give the results of a compositional analysis based on spec-
558 tral parameters. Unlike previous papers, the present work determines a semi-
559 quantitative estimation of the mixing coefficients of each lithology. Here we
560 do not consider the spectral slope or the reflectance, and thus we cannot
561 establish the specific nature of this featureless endmember. However, by
562 examining the albedo of each BM unit, we can make inferences about the
563 identity of the featureless phase.

564 We find that in general, the mixing coefficient of the featureless endmember

565 is anticorrelated with albedo, suggesting that this component is a low-albedo
566 opaque material. In fact, bright areas are often contaminated by dark ma-
567 terial (Jaumann et al., 2012; Palomba et al., 2014). In Fig. 11, we show the
568 main results from the linear unmixing model plotted on the compositional
569 map from Ammannito et al. (2013b). The mixing coefficients of the different
570 components obtained by the model and the distribution of the BM units are
571 generally in good agreement with previous analyses (e.g., De Sanctis et al.,
572 2012a, 2013b; Zambon et al., 2014). First, in all of the BM units, both eucrite
573 and diogenite spectra are used to fit VIR spectra, reflecting the distribution
574 of those components in the regolith (De Sanctis et al., 2013a,b).

575 From the results of our analysis, we can see that several BM units are dom-
576 inated by eucrite and diogenite components (see Section 8 and Table 2). In
577 particular, we can classify these units as eucrite-rich units and diogenite-rich
578 units. A third type is olivine-rich BMs.

579 The distribution of eucrite-rich and diogenite-rich units is similar to the com-
580 position of surrounding terrains as inferred by the analysis of spectral param-
581 eters.

582 Olivine-rich BM units are associated with recognized olivine-bearing craters
583 (Ammannito et al., 2013b; Ruesch et al., 2014). Moreover, where more
584 units are seen in the same crater, they frequently belong to only one family.

585 The only exceptions are a few diogenite-rich units present on eucritic ter-
586 rains (Aelia, Canuleia, BU3, BU6), and few craters (Aelia, Canuleia, Oppia,
587 Justina, BU9) where BMs show both compositions in the same location.

588 Eucrite-rich BM units may have a mixing coefficient of eucrite as high as 44%
589 (red symbols in Fig.11). Those BM units are mostly located in the equatorial

590 region, between 90°E and 300°E longitude, and their distribution is compat-
591 ible with eucrite-rich regions (Ammannito et al., 2013a). Furthermore, they
592 can be subdivided in two populations: 1) one where the mixing coefficient of
593 diogenite is higher than the mixing coefficient of the featureless endmember
594 (diamond); 2) one where the mixing coefficient of the featureless endmember
595 is greater than the mixing coefficient of diogenite (square). Those subgroups
596 are equally distributed in number and by geograpy.

597 In eucrite-rich BM units, the olivine component was never used to fit the
598 spectra. This is consistent with the rare appearance of olivine, as secondary
599 mineral, in eucrite meteorites (Mittlefehldt et al., 1998). There is just one
600 exception, the crater wall material in BU2 (BU2 CWM in Table 2), where
601 the BM is fitted by the Serra de Mage eucrite spectrum (86%), with almost
602 negligible contribution from olivine and the featureless endmember. This is
603 also the only unit where both eucrite and diogenite spectra were not selected.
604 Note that the Serra de Mage eucrite shows spectral characteristics very close
605 to howardite spectra. The spectra of this eucrite is selected only in one other
606 case: the model for an anomalous diogenite rich-units (Canuleia SM) where
607 only HED spectra were used to model the data.

608 The diogenite-rich BMs are characterized by the association of the highest
609 mixing coefficient of diogenite spectra (yellow symbols in Fig.11), with a
610 lower threshold of 40%, except for the crater wall unit in BU9 (37%). The
611 distribution of diogenite-rich BMs is widespread in longitude and in latitude,
612 extending farther to the south than eucrite-rich units. The distribution of
613 diogenite-rich BMs is also consistent with the results of previous works and
614 the spectral parameter maps, and they are generally correlated with dio-

615 genitic and howarditic terrains (Ammannito et al., 2013a).

616 Only two regions show diogenite-rich bright materials, within eucrite ter-
617 rains, the Aelia unit and the units around 300°E, where are concentrated
618 BU3, BU6, and the Canuleia unit. The diogenite-rich BM units can be dif-
619 ferentiated by the presence of the eucrite (diamonds in Fig. 11) or another
620 components (square) as the second spectra in the unmixing solutions. Unlike
621 eucrite-rich BM units, the sub-group with the spectra of eucrites selected as
622 the second component is the most frequent, whereas few units are character-
623 ized by a non-HED component selected as the second endemember.

624 Moreover, in various cases ($\sim 8.6\%$) olivine was used instead of the fea-
625 tureless component (white points within diogenite-rich BMs), even if with
626 mixing coefficient lower than 30%, with the exception of the crater wall unit
627 in Calpurnia (35%). Aelia and Canuleia craters are both in eucritic terrains
628 and they show both eucrite-rich and diogenite-rich BM locations. Aelia has
629 diogenite-rich type 1 BMs on the wall, whereas the radial material (RM)
630 is eucrite-rich. This could indicate that the Aelia impact exposed diogenite
631 blocks from greater depths, whereas fresh eucritic material that originally
632 resided close to or at the surface was ejected to form the radial material.
633 In Canuleia, we have both type 1 and 2 BMs with eucrite and diogenite
634 compositions, but the differences between the two HED components are less
635 than 64%, indicating an homogeneous distribution of eucrite and diogenite
636 components, i.e., howarditic.

637 Only one Aelia BM unit, the RM, shows a clear eucrite-rich composition.
638 Thus, even in this location, diogenite material could have been exposed by the
639 impact and mixed with eucrite (i.e., formation of howarditic breccia blocks),

640 while some eucrite-rich fresh material was ejected from the crater, and de-
641 posited on the surrounding eucritic crust.

642 In contrast, BU3 and BU6 craters show both diogenite-rich units as RM
643 (BU6 has also a SM, see Table 2). Those units are very close to the diogenite
644 terrains, so perhaps the presence of diogenite-rich material can be attributed
645 to contributions from southern craters. Alternately, it could be that the eu-
646 critic crust in that area is thinner, and thus fresh diogenitic material was
647 more easily excavated and ejected from those craters.

648 Three other craters (Oppia, BU9 crater, and Justina) show the presence of
649 both eucrite- and diogenite-rich BMs. Oppia and BU9 show both units. In
650 the Oppia crater, two BM units are on the wall. The CWM are diogenite-
651 enriched, whereas the corresponding slope material (SM) is characterized by a
652 higher amount of eucrite. In the second crater (BU9), the CWM is diogenite-
653 rich, whereas a RM BM unit is fitted by a high mixing coefficient of eucrite.
654 BM units at crater Justina have been covered by VIR more than one time,
655 the four wall units (both CWM and SM) are eucrite-rich and the two RM
656 are diogenite-rich BM units. A third family is made of olivine-rich bright
657 units, i.e., where olivine spectra are selected as the most abundant compo-
658 nent. In this family, all of the recognized BMs are enriched in olivine, with
659 diogenite > eucrite in BU14 and eucrite > diogenite in Arruntia and Bellicia
660 areas. These proportions are in agreement with those found by analysis of
661 spectral parameters in Zambon et al. (2014). These units are located in the
662 northern hemisphere and correspond to the olivine-bearing sites detected by
663 Ammannito et al. (2013b) and Ruesch et al. (2014). For Bellicia and BU14,
664 we find an olivine mixing coefficient around of $\sim 50\%$, with slightly lower

665 values found in Arruntia. These values indicate that olivine is a dominant
666 component in these sites (Ammannito et al., 2013b).

667 High abundances of olivine are generally expected to be present in man-
668 tle and plutonic rocks, which could be present in topographically low areas.
669 In this work, we have employed Mg-rich olivine endmembers with very fine
670 particle sizes, compatible with the predicted Vesta dominant regolith size.
671 Therefore, the absolute abundance values could be lower than suggested by
672 our models, in particular considering that olivine is more fayalitic (Fe-rich)
673 in HEDs. Olivine that is richer in iron has a stronger absorption band, and
674 hence a lower abundance of such Fe-rich olivine (relative to Mg-rich olivine)
675 would be needed to model a given spectrum.

676 Poulet et al. (2015) discussed the retrieval of composition from VIR spec-
677 tra by using a non-linear method (Shkuratov et al., 1999). It should be noted
678 that the results from a non-linear technique, although in principle better than
679 those from a linear model, can suffer if the starting data has not been prop-
680 erly treated. For the VIR dataset, extreme care must be taken, for example,
681 in bridging the sections VIS and IR, exclusion of spectral channels suffering
682 from recurring artifacts, and removal of the continuum. Poulet et al. (2015)
683 concluded that coarse-grained olivine is likely to be present in all major units
684 of Vesta. In general, they also found that the abundance of olivine could be
685 lower because of the presence of iron-rich olivine or because of an increase
686 in the grain size of olivine with respect to the other phases. An alterna-
687 tive hypothesis that could explain higher surface abundances of olivine in
688 such northern locations is an exogenic origin - e.g., material delivered by
689 an olivine-rich impactor, as suggested by Le Corre et al. (2015). Moreover,

690 we find that in those terrains the third selected endmember is frequently a
691 featureless component.

692 As discussed above, the mixing coefficient of the featureless endmember is
693 anti-correlated with the albedo, suggesting that this component is associated
694 with low-albedo CC-like opaque material. In fact, bright areas are often con-
695 taminated by dark material (Jaumann et al., 2012; Palomba et al., 2014).
696 We do find one exception where a BM unit with a large mixing coefficient
697 for the featureless endmember, BU15-SM, has the highest albedo (Zambon
698 et al., 2014). This unit is matched by a diogenite-rich bright unit extending
699 into the Rheasilvia basin, and Zambon et al. (2014) predicted the possible
700 presence of a bright component.

701 The major bright, iron-poor, mineral in HEDs and in basic igneous compo-
702 sition is plagioclase, which can have a large abundance in magmatic rocks,
703 both effusive and cumulitic, intrusive rocks. Plagioclase can exhibit a char-
704 acteristic absorption at $1.25\mu\text{m}$ caused by impurity iron at abundances cor-
705 responding to $\text{FeO} < 1\%$ (e.g. Burns, 1993; Cheek et al., 2011; Serventi
706 et al., 2013). However, the $1.25\mu\text{m}$ feature cannot be recognized in mixtures
707 with mafic iron-bearing silicates unless the plagioclase is present in very large
708 amounts. If plagioclase is indeed revealed by our analysis, it should be noted
709 that in HEDs it is generally present in eucrites and cumulitic eucrites, but
710 not in diogenites.

711 Another important aspect showed by our results is the selection of olivine
712 spectra with low mixing coefficient for the diogenite-rich BM units, in place
713 of the featureless endmember. From a spectroscopic viewpoint, this implies
714 that reductions of the intensities of band I and band II are not correlated,

715 otherwise the model should have selected the featureless spectrum. In ad-
716 dition, a weak asymmetry around the $1\text{-}\mu\text{m}$ absorption is revealed, so the
717 selection of only eucrite and diogenite spectra alone is not able to properly
718 fit VIR data in that specific spectral region. The presence of this low amount
719 of olivine in the diogenite-rich BM units indicates that iron could be present
720 in one or more phases with a band around $1\ \mu\text{m}$ but with a very weak, or
721 absent, absorption around $2\ \mu\text{m}$. In general, these spectral characteristics
722 are consistent with the presence of olivine, high-Ca pyroxene, plagioclase or
723 a glassy component, in basic igneous compositions.

724 Iron-bearing silicate glasses (e.g., volcanic or impact glasses) have a dom-
725 inant crystal-field absorption at $\sim 1.1\ \mu\text{m}$, the intensity of which depends
726 on the iron abundance. Thus a glassy component cannot be excluded in
727 units that are formed by impacts. In fact, impact melts have been identified
728 in some HEDs (see e.g., Metzler and Stoffer, 1995; Singerling et al., 2013).
729 High-Ca pyroxenes are not abundant in diogenite s, even if there are samples
730 where they are found in abundance higher than 10% (e.g., Mittlefehldt et al.,
731 1998). High-Ca pyroxene can also be frequently found as exsolution lamellae
732 in orthopyroxene crystals, influencing the spectral characteristics of the host
733 low-Ca hosting pyroxene (Gaffey et al., 2002).

734 Olivine is difficult to detect, especially in small amounts. The shape and
735 the position of the $1\ \mu\text{m}$ band are influenced by the presence of olivine if it
736 is present in high amounts in mixtures with pyroxene (e.g. in particular the
737 orthopyroxene-olivine mixtures studied by Cloutis et al., 1986; Beck et al.,
738 2013).

739 Beck et al. (2013) argued that olivine could be recognized only at contents

740 > 30% in HEDs, because under this threshold, the olivine is masked in
741 mixtures with orthopyroxene. (Beck et al., 2013) predicted that olivine in
742 diogenite and harzburgite terrains could not be detected when present in
743 amounts below this threshold. Recent studies by Horgan et al. (2014) and
744 Shestopalov et al. (2015) suggest two different methods for detection of small
745 amounts of olivine in mixtures with pyroxene. Horgan et al. (2014) used dif-
746 ferent spectral indices to identify the presence of olivine in the spectra of
747 Mars. Shestopalov et al. (2015) observed that the uncertainty (variance) of
748 the band center position in spectra of laboratory olivine-pyroxene mixtures
749 depends on the shift of the band center at 950 nm. They found that mixtures
750 with different olivine contents can be identified by their position in a plot of
751 the variance vs. band center at 950 nm.
752 On the other hand, Poulet et al. (2015) concluded that best fits to all the stud-
753 ied Vesta terrains are achieved when a component of forsteritic olivine (Fo70)
754 is included. They also emphasized that the particle size has an effect on the
755 olivine abundance obtained by a non-linear unmixing method. Olivine-rich
756 melts were recently found in some howardites (Beck et al., 2013), so we can-
757 not rule out that those BM units could have low olivine mixing coefficient.

758 FIGURE 11

759

760 7. Conclusions

- 761 1. To model VIR data for Vesta, we applied a linear spectral unmixing
762 model. Our analysis does not take into account the spectral slope and
763 the albedo but only the spectral shape.

- 764 2. Tests on laboratory mixtures of olivine and low- and high-calcium py-
765 roxene indicate that olivine mixing coefficients are underestimated with
766 an accuracy within 10% for olivine amounts $> 50\%$. For mixtures
767 of plagioclase with low- and high-calcium pyroxenes, the plagioclase
768 amount is underestimated within 11% for plagioclase contents $> 40\%$.
769 Analysis of mixtures of Millbillillie eucrite with carbonaceous chondrite
770 (CC) material indicates that the CC abundance was overestimated by
771 up to 26%.
- 772 3. Linear unmixing applied to Vesta spectra is able to detect the principal
773 HED and non-HED lithologies present on the asteroid.
- 774 4. We can divide the bright material units into three main groups: eucrite-
775 rich, diogenite-rich, and olivine-rich, depending on the most abundant
776 endmember used to fit the spectrum. The non-HED endmember can
777 be either olivine or a featureless component. This confirms that Vesta
778 is composed of a high content of pyroxenes mixed with a lower concen-
779 tration of other mineralogical phases.
- 780 5. The third endmember is often the featureless phase, which is associated
781 with a reduction in the strength of both pyroxene bands. The mixing
782 coefficient of the featureless endmember is anticorrelated with albedo,
783 suggesting that the featureless phase can be associated with low-albedo,
784 CC-like opaque material.
- 785 6. Large amounts of olivine are detected in the Bellicia, Arruntia and
786 BU14 BM units. Where lower olivine contents ($< 30\%$) are found, the
787 sites are generally associated with high concentrations of diogenite.

788 **Figure and Table captions**

789 **Figure 1:** Example of VIR spectrum before (top) and after (bottom) the
790 removal of the slope.

791 **Figure 2:** Spectral parameter plots for the diogenite and eucrite lab-
792 oratory samples. The gray circles indicate the samples selected for use as
793 endmembers in this study. The numbers refer to the endmember names in
794 Table 1.

795 **Figure 3:** Spectra of the endmembers selected. The text labels refer
796 to the sample names in Table 1 (6e Bereba, 7e Bouvante, 8e Cachari, 20e
797 Padvarninkai, 22e Serra de Mage, 24e Y74450, 2d ALH77256, 5d GRO95555,
798 6d Johnstown, 8d Tatahouine, 10d Y75032, 1o Jackson cty, 2o Green olivine).

799 **Figure 4:** Frequency of the endmembers for the linear unmixing with
800 two endmembers.

801 **Figure 5:** Linear unmixing applied to a mixture of olivine with low and
802 high calcium pyroxene. The band centers of the modeled spectra are shifted
803 slightly with respect to those of the laboratory spectra. In cases where the
804 χ^2 values differ from 0, there is an imperfect match between the measured
805 and modeled spectra.

806 **Figure 6:** The results of linear unmixing applied to the Aelia BM unit for
807 the 10 cases with the lowest χ^2 . These results indicate that small variations in
808 χ^2 do not correlate with changes in the endmembers or with large variations
809 in the mixing coefficients of the endmembers, attesting to the stability of the
810 results. Black lines are the measured spectra, the gray lines are the model
811 mixture spectra.

812 **Figure 7:** Frequency of the endmembers selected for the linear unmixing

813 with three endmembers.

814 **Figure 8:** Plots of band centers vs. eucrite mixing coefficients show that
 815 eucrite content increases for increasing band center values. Right: Similar
 816 plots for band centers and diogenite mixing coefficients indicates that dio-
 817 genite content decreases with increasing band center values. Band center
 818 values for the BM units are those calculated in Zambon et al. (2014). The
 819 coefficient of determination (i.e., the squared correlation coefficient R^2) is
 820 also provided.

821 **Figure 9:** Examples of linear spectral unmixing applied to BM units.
 822 Black lines are the measured spectra, the gray lines are the model mixture
 823 spectra. Table 1 summarizes the model endmember mixing coefficients for
 824 all the BM units. Related plots are presented in the SOM.

825 **Figure 10:** The albedo of each BM location plotted against the modeled
 826 mixing coefficient of the featureless endmember. As albedo decreases, the
 827 mixing coefficient of the featureless endmemeber increases.

828 **Figure 11:** Results obtained for the linear unmixing applied to BM
 829 units overlain on a mineralogical map of Vesta. Red color indicates eucrite-
 830 rich units, yellow color designates the diogenite-rich units, and the white
 831 symbols are the olivine-rich bright materials. Diamonds indicate BM units
 832 for which the eucrite or diogenite mixing coefficient is larger than that of
 833 the third endmember. Squares correspond to BM in which the eucrite or
 834 diogenite amount is lower than that of the third component. The solid white
 835 points are BM units with olivine as the third endmember (See also Table
 836 2). The legend at the top refers to the different cases found in our analysis.
 837 For example, "D>III" indicates that the mixing coefficient of the diogenite

838 is greater than those of the third component. "E>III" represents the cases
839 in which the mixing coefficient of the eucrite is greater than that of the third
840 endmember, and so on

841 **Table 1:** Sample name, type, band centers, and band depths for all the
842 endmembers in our spectral library. Each spectrum is assigned an identifi-
843 cation number that contains "e" for eucrite, "d" for diogenite, and "o" for
844 olivine.

845 **Table 2:** Summary of the results obtained from application of linear
846 spectral unmixing on BM units on Vesta. Endmembers are designated as
847 eucrite ("E"), diogenite ("D"), or olivine ("Ol"), while "Line" refer to the
848 featureless component. Different text color and box color are indicative of
849 variations in composition: Red text refers to eucrite-rich BM units where
850 the featureless endmember (line) is the second most abundant. Yellow text
851 indicates diogenite-rich endmember in which the second most abundant end-
852 member is either the featureless one or olivine. Green text represents cases
853 with olivine as the non-HED spectrum. Red boxes correspond to eucrite-rich
854 BM units with diogenite as the second most abundant endmember. Yellow
855 boxes are diogenite-rich BM units with eucrite as the second most abundant
856 endmember. Green boxes represent the olivine-rich BM units. In the last
857 column are reported the values of the correlation coefficient r .

858

859 Acknowledgments

860 VIR is funded by the Italian Space Agency-ASI and was developed under
861 the leadership of INAF-Istituto di Astrofisica e Planetologia Spaziale, Rome-

862 Italy. The instrument was built by Selex-Galileo, Florence-Italy. The authors
863 acknowledge the support of the Dawn Science, Instrument, and Operations
864 Teams. This work was supported by ASI and NASA's.

865 Adams, J. B., Smith, D. E., Johnson, T. V., 1986. Spectral mixture
866 modeling: A new analysis of rock and soil types at the Viking
867 Lander 1 site. *Journal of Geophysical Research* 91, 8098–8112. DOI:
868 10.1029/JB091iB08p08098.

869 Ammannito, E., De Sanctis, M. C., Capaccioni, F., Capria, M., Carraro, F.,
870 Combe, P., J., Fonte, S., Frigeri, A., Joy, S., Longobardo, A., Magni, G.,
871 McCord, T. B., McFadden, L. A., McSween, H., Palomba, E., Pieters, C.,
872 P., C., Raymond, C. A., Sunshine, J., Tosi, F., Zambon, F., Russell, C. T.,
873 2013a. Vestan lithologies mapped by the visual and infrared spectrome-
874 ter on Dawn. *Meteoritics & Planetary Science* 48 (11), 2185–2198. DOI:
875 10.1111/maps.12192.

876 Ammannito, E., De Sanctis, M. C., Palomba, E., Longobardo, A., Mittle-
877 fehldt, D. W., McSween, H. Y., Marchi, S., Capria, M. T., Capaccioni,
878 F., Frigeri, A., Pieters, C. M., Ruesch, O., Tosi, F., F., Z., Carraro, F.,
879 Fonte, S., Hiesinger, H., Magni, G., McFadden, L. A., Raymond, C. A.,
880 C.T., R., Sunshine, J. M., 2013b. Olivine from vesta's mantle exposed on
881 the surface. *Nature* 504, 122–125. DOI: 10.1038/nature12665.

882 Beck, A. W., McCoy, T. J., Sunshine, J. M., Viviano, C. E., Corrigan, C. M.,
883 Hiroi, T., Mayne, R. G., 2013. "challenges in detecting olivine on the
884 surface of 4 vesta". *Meteoritics & Planetary Science* 48 (11), 2155–2165.
885 DOI: 10.1111/maps.12160.

- 886 Beck, A. W., McSween, H. Y., 2010. Diogenites as polymict breccias com-
887 posed of orthopyroxenite and harzburgite. *Meteoritics & Planetary Science*
888 45, 850–872. DOI: 10.1111/j.1945–5100.2010.01061.x.
- 889 Beck, A. W., McSween, H. Y., Viviano, C. E., 2011. Petrologic and textural
890 diversity in one of the largest samples of the vestan regolith. 74th Annual
891 Meeting of the Meteoritical Society.
- 892 Binzel, R. P., Gaffey, M. J., Thomas, P. C., Zellner, B. H., Storrs, A. D., W.
893 E. N., 1997. Geologic Mapping of Vesta from 1994 Hubble Space Telescope
894 Images. *Icarus* 128, 95–103. DOI: 10.1006/icar.1997.5734.
- 895 Bioucas-Dias, J. M., Plaza, A., Dobigeon, N., Parente, M., Du, Q., Gader,
896 P., Chanussot, J., 2012. Hyperspectral Unmixing Overview: Geometrical,
897 Statistical, and Sparse Regression-Based Approaches. *IEEE JOURNAL OF*
898 *SELECTED TOPICS IN APPLIED EARTH OBSERVATIONS AND RE-*
899 *MOTE SENSING* 5, 354–379. DOI: 10.1109/JSTARS.2012.2194696.
- 900 Blewett, D. T., Hawke, B., Lucey, P. G., Taylor, L. A., Jaumann, R., Spudis,
901 P. D., 1995. Remote sensing and geologic studies of the Schiller-Schickard
902 region of the Moon. *Journal of Geophysical Research* 100 (E8), 16959–
903 16978. DOI: 10.1029/95JE01409.
- 904 Bobrovnikoff, N. T., 1929. The spectra of minor planets. *Lick Ob-*
905 *servatory bulletin*. University of California Press 407, 18–27. DOI:
906 10.5479/ADS/bib/1929LicOB.14.18B.
- 907 Burbine, T. H., Buchanan, P. C., Dolkar, T., Binzel, R. P., 2009. Pyroxene

- 908 mineralogies of near-Earth vestoids. *Meteoritics & Planetary Science* 44,
909 1331–1341. DOI: 10.1111/j.1945–5100.2009.tb01225.x.
- 910 Burns, R., 1993. *Mineralogical Applications of Crystal Field Theory*. Second
911 Edition. Cambridge University Press.
- 912 Cheek, L. C., Pieters, C. M., Boardman, J. W., Clark, R. N., Combe, J.-
913 P., Head, J. W., Isaacson, P., McCord, T. B., Moriarty, D., Nettles, J.,
914 Petro, N., Sunshine, J. M., Taylor, L. A., 2011. "goldschmidt crater and
915 the moon's north polar region: Results from the moon mineralogy mapper
916 (m3)". *Journal of Geophysical Research* 116, DOI: 10.1029/2010JE003702.
- 917 Clark, R. N., 1999. *Remote Sensing for the Earth Sciences - Manual of Re-*
918 *remote Sensing*. Vol. 3. John Wiley and Sons, New York.
- 919 Cloutis, E. A., Gaffey, M. J., Jackowski, T. L., Reed, K. L., 1986. Calibrations
920 of phase abundance, composition, and particle size distribution for olivine-
921 orthopyroxene mixtures from reflectance spectra. *Journal of Geophysical*
922 *Research* 91, 641–653. DOI: 10.1029/JB091iB11p11641.
- 923 Cloutis, E. A., Izawa, M. R. M., Pompilio, L., Reddy, V., Hiesinger, H.,
924 Nathues, A., Mann, P. J., Le Corre, L., Palomba, E., Bell, J. F., 2013.
925 Spectral reflectance properties of HED meteorites + CM2 carbonaceous
926 chondrites: Comparison to HED grain size and compositional variations
927 and implications for the nature of low-albedo features on Asteroid 4 Vesta.
928 *Icarus* 223, 850–877. DOI: 10.1016/j.icarus.2013.02.003.
- 929 Combe, J.-P., Le Moulic, S., Sotin, C., Gendrin, A., Mustard, J. F., Le Deit,
930 L., Launeau, P., Bibring, L.-P., Gondet, B., Langevin, Y., Pinet, P., the

931 Omega Science team, 2008. "analysis of omega/mars express data hyper-
932 spectral data using a multiple-endmember linear spectral unmixing model
933 (melsum): Methodology and first results". *Planetary and Space Science*
934 56 (7), 951–975. DOI: 10.1016/j.pss.2007.12.007.

935 Consolmagno, G. J., Drake, M. J., 1977. Composition and evolution of the
936 eucrite parent body - Evidence from rare earth elements. *Geochimica et*
937 *Cosmochimica Acta* 41, 1271–1282. DOI: 10.1016/0016-7037(77)90072-2.

938 Dalton, J. B. I., 2007. Linear mixture modeling of Europa's non-ice material
939 based on cryogenic laboratory spectroscopy. *Geophysical Research Letters*
940 34 (L21205), DOI: 10.1029/2007GL031497.

941 Dalton, J. B. I., Shirley, J. H., Cassidy, T., Paranicas, C. J., Kamp, L. W.,
942 2011. Spectral properties of hydrated sulfate minerals on mars spectral
943 properties of hydrated sulfate minerals on mars spectral properties of hy-
944 drated sulfate minerals on mars. EPSC-DPS.

945 De Sanctis, M., Ammannito, E., Capria, M., Tosi, F., F., Z., Carraro, F.,
946 Fonte, S., Frigeri, A., Jaumann, R., Magni, G., Marchi, S., McCord,
947 T. B., McFadden, L., McSween, H. Y., Mittlefehldt, D. W., Nathues, A.,
948 Palomba, E. P., C.M., Raymond, C., Russell C.T. andToplis, M. J., Tur-
949 rini, D., 2012a. Spectroscopic Characterization of Mineralogy and Its Di-
950 versity Across Vesta. *Science* 336, 697–700. DOI: 10.1126/science.1219270.

951 De Sanctis, M., Ammannito, E., Palomba, E., Longobardo, A., Capaccioni,
952 F., Frigeri, A., Tosi, F., F., Z., Capria, M., Marchi, S., Magni, G., McFad-

953 den, L., McSween, H., Pieters, C., Raymond, C., C.T., R., 2013a. Possible
954 detection of olivine on vesta. 44th LPSC.

955 De Sanctis, M., Coradini, A., Ammannito, E., Filacchione, G., Capria, M.,
956 Fonte, S., Magni, G., Barbis, A., Bini, A., Dami, M., Fikai-Veltroni, I.,
957 Preti, G., the VIR Team, 2011. The VIR Spectrometer. *Space Science*
958 *Reviews* 163, 329–369. DOI: 10.1007/s11214-010-9668-5.

959 De Sanctis, M. C., Ammannito, E., Capria, M. T., Capaccioni, F., Combe,
960 J.-P., Frigeri, A., Longobardo, A., Magni, G., Marchi, S., McCord, T. B.,
961 Palomba, E., Tosi, F., Zambon, F., Carraro, F., Fonte, S., Li, J.-Y., Mc-
962 Fadden, L. A., Mittlefehldt, D. W., Pieters, C. M., Jaumann, R., Stephan,
963 K., Raymond, C. A., Russell, C. T., 2013b. Vesta's mineralogical com-
964 position as revealed by the visible and infrared spectrometer on Dawn.
965 *Meteoritics & Planetary Science*, DOI: 10.1111/maps.12138.

966 De Sanctis, M. C., Combe, J.-P., Ammannito, E., Palomba, E., Longobardo,
967 A., McCord, T. B., Marchi, S., Capaccioni, F., Capria, M. T., Mittlefehldt,
968 D. W., Pieters, C. M., Sunshine, J., Tosi, F., Zambon, F., Carraro, F.,
969 Fonte, S., Frigeri, A., Magni, G., Raymond, C. A., Russell, C. T., Turrini,
970 D., 2012b. Detection of widespread hydrated materials on Vesta by the VIR
971 imaging spectrometer on board the DAWN mission. *The Astrophysical*
972 *Journal Letters* 758, L36. DOI:10.1088/2041-8205/758/2/L36.

973 Donaldson Hanna, K., Sprague, A. L., 2009. Vesta and the hed meteorites:
974 Mid-infrared modeling of minerals and their abundances. *Meteoritics &*
975 *Planetary Science* 44 (11), 1755–1770. DOI:

- 976 Feierberg, M. A., Drake, M. J., 1980. The meteorite-asteroid connection - The
977 infrared spectra of eucrites, shergottites, and Vesta. *Science* 209, 805–807.
978 DOI: 10.1126/science.209.4458.805.
- 979 Fox III, L., Fischer, A. F., Gillespie, A. R., Smith, M. R., 1990. "using
980 spectral mixture analysis of aviris high dimensional data for distinguishing
981 soil chronosequences". In: *Proceedings of the Airborne Science Workshop:*
982 *AVIRIS*. Jet Propulsion Laboratory.
- 983 Gaffey, M. J., Cloutis, E. A., Kelley, M. S., Reed, K. L., 2002. *Mineralogy of*
984 *Asteroids*. Asteroids III-University of Arizona Press, Tucson.
- 985 Hapke, B., 1981. Bidirectional reflectance spectroscopy. I - Theory. *Journal*
986 *of Geophysical Research* 86, 3039–3054. DOI: 10.1029/JB086iB04p03039.
- 987 Hapke, B., 1993. *Theory of Reflectance and Emittance Spectroscopy*.
- 988 Hiroi, T., Pieters, C. M., Takeda, H., 1994. Grain size of the surface regolith
989 of asteroid 4 Vesta estimated from its reflectance spectrum in comparison
990 with HED meteorites. *Meteoritics* 29 (394-396.).
- 991 Horgan, B. H. N., Cloutis, E. A., Mann, P. J., Bell, J. F. I., 2014.
992 Near-infrared spectra of ferrous mineral mixtures and methods for their
993 identification in planetary surface spectra. *Icarus* 234, 132–154. DOI:
994 10.1016/j.icarus.2014.02.031.
- 995 Jaumann, R., Williams, D. A., Buczkowski, D., Yingst, R., Preusker, F.,
996 Hiesinger, H., Schmedemann, N., Kneissl, T., Vincent, J. B., Blewett,
997 D. T., Buratti, B. J., Carsenty, U., Denevi, B. W., De Sanctis, M. C.,

- 998 Garry, W., Keller, H. U., Kersten, E., Krohn, K., Li, J.-Y., Marchi, S.,
999 Matz, K.-D., McCord, T. B., McSween, H. Y., Mest, S., Mittlefehldt,
1000 D. W., Mottola, S., Nathues, A., Neukum, G., O'Brien, D. P., Pieters,
1001 C. M., Prettyman, T. H., Raymond, C. A., Roatsch, T., C.T., R., Schenk,
1002 P., Schmidt, B. E., Scholten, F., Stephan, K., Sykes, M. V., Tricarico, P.,
1003 Wagner, R., Zuber, M. T., Sierks, H., 2012. Vesta's Shape and Morphology.
1004 Science 336, 687. DOI: 10.1126/science.1219122.
- 1005 Keshava, N., Mustard, J., 2002. Spectral unmixing. IEEE Signal Processing
1006 Magazine 19 (1), 44–57. DOI: 10.1109/79.974727.
- 1007 Lawrence, D. J., Peplowski, P. N., Prettyman, T. H., William, C., Feldman,
1008 W. C., Bazell, D., Mittlefehldt, D. W., Reedy, R. C., Yamashita, N., 2013.
1009 "constraints on vesta's elemental composition: Fast neutron measurements
1010 by dawn's gamma ray and neutron detector". Meteoritics & Planetary
1011 Science 48 (11), 2271–2288. DOI: 10.1111/maps.12187.
- 1012 Le Corre, L., Reddy, V., Sanchez, J. A., Dunn, T., Cloutis, E. A., Izawa, M.
1013 R. M., Mann, P. J., Nathues, A., 2015. "exploring exogenic sources for the
1014 olivine on asteroid (4) vesta". Icarus, DOI: 10.1016/j.icarus.2015.01.018.
- 1015 Le Corre, L., Reddy, V., Schmedemann, N., Becker, K. J., O'Brien, D. P.,
1016 Yamashita, N., Peplowski, P. N., Prettyman, T. H., Prettyman, T. H., Li,
1017 J. Y., Cloutis, E. A., Denevi, B. W., Kneissl, T., Palmer, E., Gaskell, R.,
1018 Nathues, A., Gaffey, M. J., Mittlefehldt, D. W., Garry, W., Sierks, H.,
1019 Russell, C., Raymond, C. A., De Sanctis, M. C., Ammannito, E., 2013.
1020 "olivine or impact melt: Nature of the "orange" material on vesta from
1021 dawn". Icarus 226 (2), 1568–1594. DOI: 10.1016/j.icarus.2013.08.013.

- 1022 Li, J. Y., McFadden, L. A., Thomas, P. C., Mutchler, M. J., Parker, J. W.,
1023 Young, E., F., Russell, C., Sykes, M. V., Schmidt, B. E., 2010. Photometric
1024 mapping of asteroid (4) Vesta's southern hemisphere with Hubble Space
1025 Telescope. *Icarus* 208, 238–251. DOI: 10.1016/j.icarus.2010.02.008.
- 1026 Li, J.-Y., Mittlefehldt, D. W., Pieters, C. M., De Sanctis, M. C., Schröder,
1027 S. E., Hiesinger, H., Blewett, D. T., C.T., R., Raymond, C. A., Keller,
1028 H. U., 2012. INVESTIGATING THE ORIGIN OF BRIGHT MATERI-
1029 ALS ON VESTA: SYNTHESIS, CONCLUSIONS, AND IMPLICATIONS.
1030 LPSC.
- 1031 Longobardo, A., Palomba, E., Capaccioni, F., De Sanctis, M. C., Tosi, F.,
1032 Ammannito, E., Schröder, S. E., Zambon, F., Raymond, C., A., Russell,
1033 C., 2014. Photometric behavior of spectral parameters in Vesta dark and
1034 bright region as inferred by the Dawn VIR spectrometer. *Icarus* 240, 20–35.
1035 DOI: 10.1016/j.icarus.2014.02.014.
- 1036 Lupishko, D. F., Bel'Skaia, I. N., Kvaratskheliia, O. I., Kiselev, N. N., Mo-
1037 rozhenko, A. V., 1988. The polarimetry of Vesta during the 1986 opposition.
1038 *Astronomicheskii Vestnik* 22 (142-146).
- 1039 Mayne, R. G., Sunshine, J. M., McSween, H. Y., McCoy, T. J., Corrigan,
1040 C. M., Gale, A., 2010. Petrologic insights from the spectra of the unbrec-
1041 ciated eucrites: Implications for Vesta and basaltic asteroids. *Meteoritics &*
1042 *Planetary Science* 45, 1074–1092. DOI: 10.1111/j.1945–5100.2010.01090.x.
- 1043 McCord, T. B., Adams, J. B., Johnson, T. V., 1970. Asteroid Vesta: Spectral

1044 Reflectivity and Compositional Implications. *Science* 168, 1445–1447. DOI:
1045 10.1126/science.168.3938.1445.

1046 McCord, T. B., Li, J.-Y., Combe, J.-P., McSween, H. Y., Jaumann, R.,
1047 Reddy, V., Tosi, F., Williams, D. A., Blewett, D. T., Turrini, D., Palomba,
1048 E., Pieters, C. M., De Sanctis, M. C., Ammannito, E., Capria, M. T.,
1049 Le Corre, L., Longobardo, A., Nathues, A., Mittlefehldt, D. W., Schroder,
1050 S. E., Hiesinger, H., Beck, A. W., Capaccioni, F., Carsenty, U., Keller,
1051 H. U., Denevi, B. W., Sunshine, J. M., Raymond, C. A., Russell, C. T.,
1052 2012. Dark material on Vesta from the infall of carbonaceous volatile-rich
1053 material. *Nature* 461, 83–86. DOI:10.1038/nature11561.

1054 McSween, H. Y., Ammannito, E., Reddy, V., Prettyman, T., H., Beck, A. W.,
1055 De Sanctis, M. C., Nathues, A., Le Corre, L., O'Brien, D. P., Yamashita,
1056 N., McCoy, T. J., Mittlefehldt, D. W., Toplis, M. J., Schenk, P., Palomba,
1057 E., Turrini, D., Tosi, F., Zambon, F., Longobardo, A., Capaccioni, F.,
1058 Raymond, C., A., Russell, C. T., 2013. Composition of the Rheasilvia
1059 basin, a window into Vesta's interior. *Journal of Geophysical Research*
1060 118, 335–346. DOI: 10.1002/jgre.20057.

1061 McSween, H. Y., Mittlefehldt, D. W., Beck, A. W., Mayne, R. G., Mc-
1062 Coy, T. J., 2011. Meteorites and Their Relationship to the Geology of
1063 Vesta and the Dawn Mission. *Space Science Reviews* 163 (141-174. DOI:
1064 10.1007/s11214-010-9637-z).

1065 Metzler, K., Stoffer, D., 1995. "impact melt rocks and granulites from the
1066 hed asteroid". *Meteoritics* 30 (5), 547.

- 1067 Mittlefehldt, D. W., Li, J.-Y., Pieters, C. M., De Sanctis, M. C., Schröder,
1068 S. E., Hiesinger, H., Blewett, D. T., Russell, C. T., Raymond, C. A.,
1069 Yingst, R., 2012. Types and Distribution of Bright Materials on 4 Vesta.
1070 LPSC.
- 1071 Mittlefehldt, D. W., McCoy, T. J., Goodrich, C. A., Kracher, A., 1998. Non-
1072 Chondritic Meteorites from Asteroids bodies. Vol. 36. Planetary Materials
1073 chapter 4.
- 1074 Palomba, E., Longobardo, A., De Sanctis, M. C., Zambon, F., Tosi, F., Am-
1075 mannito, E., Capaccioni, F., Frigeri, A., Capria, M. T., Cloutis, E. A.,
1076 Jaumann, R., Combe, J.-P., Raymond, C. A., Russell, C. T., 2014. Com-
1077 position and mineralogy of dark material deposits on Vesta. *Icarus* 240,
1078 58–72. DOI: <http://dx.doi.org/10.1016/j.icarus.2014.04.040>.
- 1079 Palomba, E., Longobardo, A., De Sanctis, M. C., Zinzi, A., Ammannito, E.,
1080 Marchi, S., Tosi, F., Zambon, F., Capria, M. T., Russell, C. T., Raymond,
1081 C. A., Cloutis, E. A., 2015. Detection of new olivine-rich locations on Vesta.
1082 *Icarus* 258 (120–134. DOI: 10.1016/j.icarus.2015.06.011).
- 1083 Pieters, C. M., Englert, A. J., 1993. "Remote geochemical analysis : ele-
1084 mental and mineralogical composition". Cambridge, England ; New York
1085 ; Press Syndicate of University of Cambridge.
- 1086 Poulet, F., Ruesch, O., Langevin, Y., Hiesinger, H., 2015. "modal
1087 mineralogy of the surface of Vesta: Evidence for ubiquitous olivine
1088 and identification of meteorite analogue". *Icarus* 253, 354–377. DOI:
1089 10.1016/j.icarus.2014.06.002.

- 1090 Prettyman, T. H., Beck, A. W., Feldman, W. C., Lawrence, D. J., McCoy,
1091 T. J., McSween, H. Y., Mittlefehldt, D. W., Peplowski, P. N., Raymond,
1092 C. A., Reedy, R. C., Russell, C. T., Titus, T. N., Toplis, M. J., Yamashita,
1093 N., 2014. "vesta's elemental composition". LPSC.
- 1094 Prettyman, T. H., Feldman, W. C., McSween, H. Y., Dingler, R. D., Ene-
1095 mark, D. C., Patrick, D. E., Storms, S. A., Hendricks, J. S., Morgenthaler,
1096 J. P., Pitman, K. M., Reedy, R. C., 2011. Dawn's Gamma Ray and Neutron
1097 Detector. *Space Science Reviews* 163, 371–459. DOI: 10.1007/s11214-011-
1098 9862-0.
- 1099 Prettyman, T. H., Mittlefehldt, D. W., Yamashita, N., Beck, A. W., Feld-
1100 man, W. C., William, C., Hendricks, J. S., Lawrence, D. J., McCoy, T. J.,
1101 Timothy, N., McSween, H. Y., Peplowski, P. N., Patrick, D. E., Reedy,
1102 R. C., Toplis, M. J., Le Corre, L., Mizzon, H., Reddy, V., Titus, T. N.,
1103 Raymond, C. A., Russell, C. T., 2013. "neutron absorption constraints
1104 on the composition of 4 vesta". *Meteoritics & Planetary Science* 48 (11),
1105 2211–2236. DOI: 10.1111/maps.12244.
- 1106 Ramsey, M. S., Christensen, P. R., 1992. "the linear "unmixing" of lab-
1107 oratory thermal infrared spectra: implications for the thermal emission
1108 spectrometer (tes) experiment, mars observer". LPSC.
- 1109 Reddy, V., Le Corre, L., O'Brien, D. P. and Nathues, a., Cloutis, E. A.,
1110 Durda, D., Bottke, W. F., B. M. U., Nervorny, D., Buczowski, D., Scully,
1111 J. E. C., Palmer, E. M., Sierks, H., Mann, P. J., Becker, K. J., Beck, A. W.,
1112 Mittlefehldt, D. W., Li, J.-Y., Gaskell, R., Russell, C. T., Gaffey, M. J.,
1113 McSween, H. Y., McCord, T. B., Combe, J.-P., Blewett, D. T., 2012a.

- 1114 Delivery of dark material to Vesta via carbonaceous chondritic impacts.
1115 *Icarus* 223, 544–559. DOI: 10.1016/j.icarus.2012.10.006.
- 1116 Reddy, V., Li, J.-Y., Le Corre, L., Scully, J. E. C., Gaskell, R., Russell,
1117 C. T., Park, R. S., Nathues, A., Gaffey, M. J., Sierks, H., Becker, K. J.,
1118 McFadden, L. A., 2013. Comparing Dawn, Hubble Space Telescope, and
1119 ground-based interpretations of (4) Vesta. *Icarus* 226, 1103–1114. DOI:
1120 10.1016/j.icarus.2013.07.019.
- 1121 Reddy, V., Nathues, A., Le Corre, L., Sierks, H., Li, J.-Y., Gaskell, R.,
1122 McCoy, T. J., Beck, A. W., Schröder, S. E., Pieters, C. M., Becker, K. J.,
1123 Buratti, B. J., Denevi, B. W., Blewett, D. T., Christensen, U., Gaffey,
1124 M. J., Gutierrez-Marques, P., Hicks, M., Keller, H. U., Maue, T., Mottola,
1125 S., McFadden, L. A., McSween, H. Y., Mittlefehldt, D. W., O'Brien, D. P.,
1126 Raymond, C. A., Russell, C. T., 2012b. Color and Albedo Heterogeneity
1127 of Vesta from Dawn. *Science* 336, 700–704. DOI: 10.1126/science.1219088.
- 1128 Reddy, V., Sanchez, J. A., Nathues, A., Moskovitz, N. A., Li, J.-Y., Cloutis,
1129 E. A., Archer, K., Tucker, R. A., Gaffey, M. J., Paul Mann, J., Sierks, H.,
1130 Schade, U., 2012c. Photometric, spectral phase and temperature effects on
1131 4 Vesta and HED meteorites: Implications for the Dawn mission. *Icarus*
1132 217, 153–168. DOI: 10.1016/j.icarus.2011.10.010.
- 1133 Roatsch, T., Kersten, E., Matz, K.-D., Preusker, F., Scholten, F., Jau-
1134 mann, R., Raymond, C. A., Russell, C. T., 2012. High resolution Vesta
1135 High Altitude Mapping Orbit (HAMO) Atlas derived from Dawn fram-
1136 ing camera images. *Planetary and Space Science* 73, 283–286. DOI:
1137 10.1016/j.pss.2012.08.021.

- 1138 Ruesch, O., Hiesinger, H., De Sanctis, M. C., Ammannito, E., Palomba,
1139 E., Longobardo, A., Zambon, F., Tosi, F., Capria, M. T., Capaccioni, F.,
1140 Frigeri, A., Fonte, S., Magni, G., Raymond, C. A., Russell, C. T., 2014.
1141 Detections and geologic context of local enrichments in olivine on Vesta
1142 with VIR/Dawn data. *Journal of Geophysical Research* 119 (9), 2078–2108.
1143 DOI: 10.1002/2014JE004625.
- 1144 Russell, C. T., Raymond, C. A., 2011. The Dawn Mission to Vesta and Ceres.
1145 *Space Science Reviews* 163, 3–23. 10.1007/s11214-011-9836-2.
- 1146 Russell, C. T., Raymond, C. A., Coradini, A., McSween, H. Y., Zuber, M. T.,
1147 Nathues, A., De Sanctis, M. C., Jaumann, R., Konopliv, A. S., Preusker,
1148 F., Asmar, S. W., Park, R. S., Gaskell, R., Keller, H. U., Mottola, S.,
1149 Roatsch, T., Scully, J. E. C., Smith, D. E., Tricarico, P., Toplis, M. J.,
1150 Christensen, U. R., Feldman, W. C., Lawrence, D. J., McCoy, T. J., Pret-
1151 tyman, T. H., Reedy, R. C., Sykes, M. E., Titus, T. N., 2012. Dawn
1152 at Vesta: Testing the protoplanetary paradigm. *Science* 336, 684–686.
1153 DOI:10.1126/science.1219381.
- 1154 Schröder, S. E., Mottola, S., Keller, H., 2013. Resolved Photometry of Vesta
1155 Reveals Physical Properties of Crater Regolith. *Planetary and Space Sci-*
1156 *ence*, DOI: dx.doi.org/10.1016/j.pss.2013.06.009.
- 1157 Serventi, G., Carli, C., Sgavetti, M., Ciarniello, M., Capaccioni, F.,
1158 Pedrazzi, G., 2013. Spectral variability of plagioclase–mafic mix-
1159 tures (1): Effects of chemistry and modal abundance in reflectance
1160 spectra of rocks and mineral mixtures. *Icarus* 226, 282–298. DOI:
1161 dx.doi.org/10.1016/j.icarus.2013.05.041.

- 1162 Shestopalov, D. I., Golubeva, L. F., Cloutis, E. A., 2015. Remote sensing
1163 olivine in pyroxene-bearing targets: The case of v-type asteroids. LPSC.
- 1164 Shestopalov, D. I., McFadden, L. A., Golubeva, L. F., Orujova, L. O., 2010.
1165 About mineral composition of geologic units in the northern hemisphere
1166 of vesta. *Icarus* 209 (2), 575–585. DOI: 10.1016/j.icarus.2010.04.012.
- 1167 Shkuratov, Y., Starukhina, L., Hoffmann, H., Arnold, G., 1999. A model of
1168 spectral albedo of particulate surfaces: Implications for optical properties
1169 of the moon. *Icarus* 137, 235–246. DOI: 10.1006/icar.1998.6035.
- 1170 Singer, R. B., McCord, T. B., 1979. Mars: Large scale mixing of bright and
1171 dark surface materials and implications for analysis of spectral reflectance.
1172 LPSC, 1835–1848.
- 1173 Singerling, S. A., McSween, H. Y., Taylor, L. A., 2013. "glasses in howardites:
1174 Impact melts or pyroclasts?". *Meteoritics & Planetary Science* 48 (5), 715–
1175 729. DOI: 10.1111/maps.12099.
- 1176 Thangjam, G., Reddy, V., Le Corre, L., Nathues, A., Sierks, H., Hiesinger,
1177 H., Li, J.-Y., Sanchez, J. A., Russell, C. T., Gaskell, R., Raymond, C. A.,
1178 2013. Lithologic mapping of hed terrains on vesta using dawn framing
1179 camera color data. *Meteoritics & Planetary Science* 48 (11), 2199–2210.
1180 DOI: 10.1111/maps.12132.
- 1181 Thomas, P. C., Binzel, R. P., Gaffey, M. J., Storrs, A., D., Wells, E. N.,
1182 Zellner, B. H., 1997. Impact Excavation on Asteroid 4 Vesta: Hub-
1183 ble Space Telescope Results. *Science* 227, 1492–1495. DOI: 10.1126/sci-
1184 ence.277.5331.1492.

- 1185 Tosi, F., Capria, M. T., De Sanctis, M. C., Combe, J.-P., Zambon, F.,
1186 Nathues, A., Schröder, S. E., Li, J.-Y., Palomba, E., Longobardo, A.,
1187 Blewett, D. T., Denevi, B. W., Palmer, E., Capaccioni, F., Amman-
1188 nito, E., Titus, T., Mittlefehldt, D. W., Sunshine, J. M., Russell, C. T.,
1189 Raymond, C., A., 2014. Thermal measurements of dark and bright sur-
1190 face features on vesta as derived from dawn/vir. *Icarus* 240, 36–57. DOI:
1191 10.1016/j.icarus.2014.03.017.
- 1192 Tosi, F., Frigeri, A., Combe, J.-P., Zambon, F., De Sanctis, M. C., Amman-
1193 nito, E., Longobardo, A., Hoffman, M., Nathues, A., Garry, W., Blewett,
1194 D. T., Pieters, C. M., Palomba, E., Stephan, K., McFadden, L. A., Mc-
1195 Sween, H. Y., Russell, C. T., Raymond, C. A., the Dawn Science Team,
1196 2015. Mineralogical analysis of the oppia quadrangle of asteroid (4) vesta:
1197 Evidence for occurrence of moderate-reflectance hydrated minerals. *Icarus*
1198 259, 129–149. DOI: 10.1016/j.icarus.2015.05.018.
- 1199 Williams, D. A., Yingst, R., Garry, W., 2014. "introduction: The geologic
1200 mapping of vesta". *Icarus* 244, 1–12. DOI: 10.1016/j.icarus.2014.03.001.
- 1201 Zambon, F., De Sanctis, M. C., Schröder, S. E., Tosi, F., Longobardo, A.,
1202 Ammannito, E., Blewett, D. T., Mittlefehldt, D. W., Li, J.-Y., Palomba,
1203 E., Capaccioni, F., Frigeri, A., Capria, M. T., Fonte, S., Nathues, A.,
1204 Pieters, C. M., Russell, C. T., Raymond, C., A., 2014. Spectral Analysis
1205 of the Bright Materials on the Asteroid Vesta. *Icarus* 240, 73–85. DOI:
1206 10.1016/j.icarus.2014.04.037.
- 1207 Zambon, F., Frigeri, A., Combe, J.-P., Tosi, F., Longobardo, A., Ammannito,
1208 E., De Sanctis, M. C., Blewett, D. T., Scully, J. E. C., Palomba, E., Denevi,

1209 B. W., Yingst, A., Russell, C. T., Raymond, C. A., 2015. Spectral analysis
1210 of the quadrangles av-13 and av-14 on vesta. *Icarus* 259, 181–193. DOI:
1211 10.1016/j.icarus.2015.05.015.

ACCEPTED MANUSCRIPT

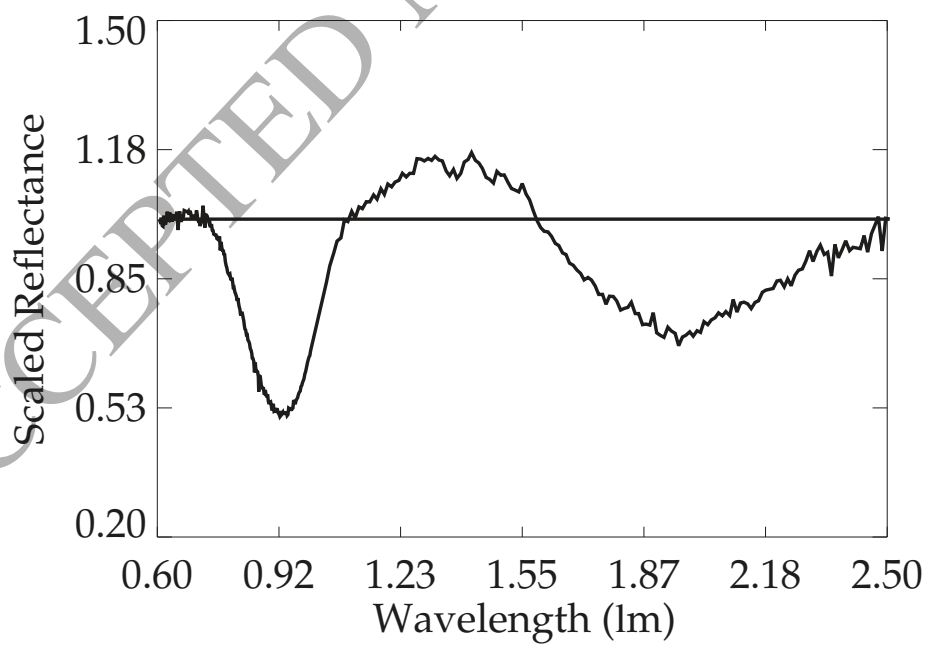
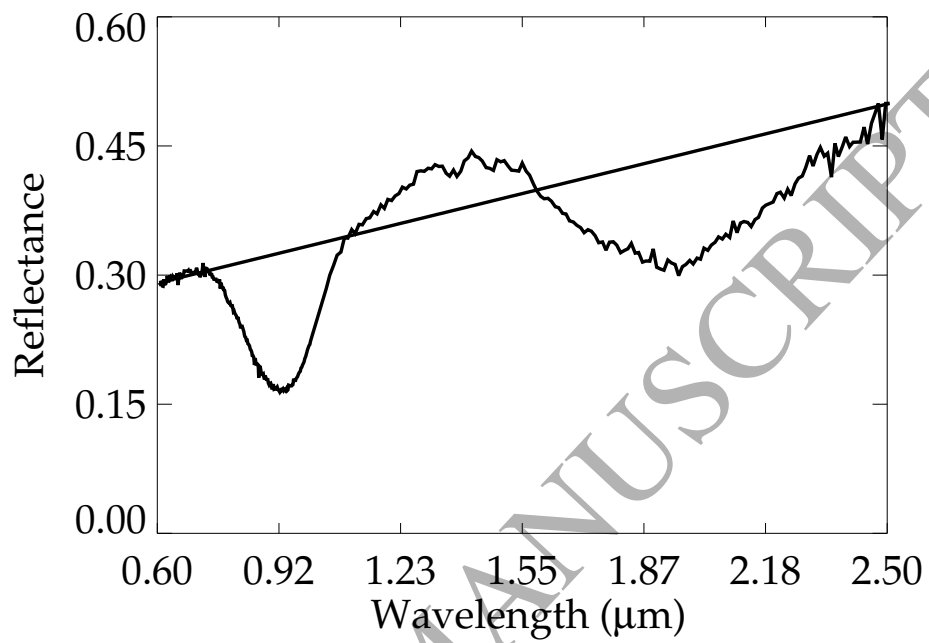


Figure 1

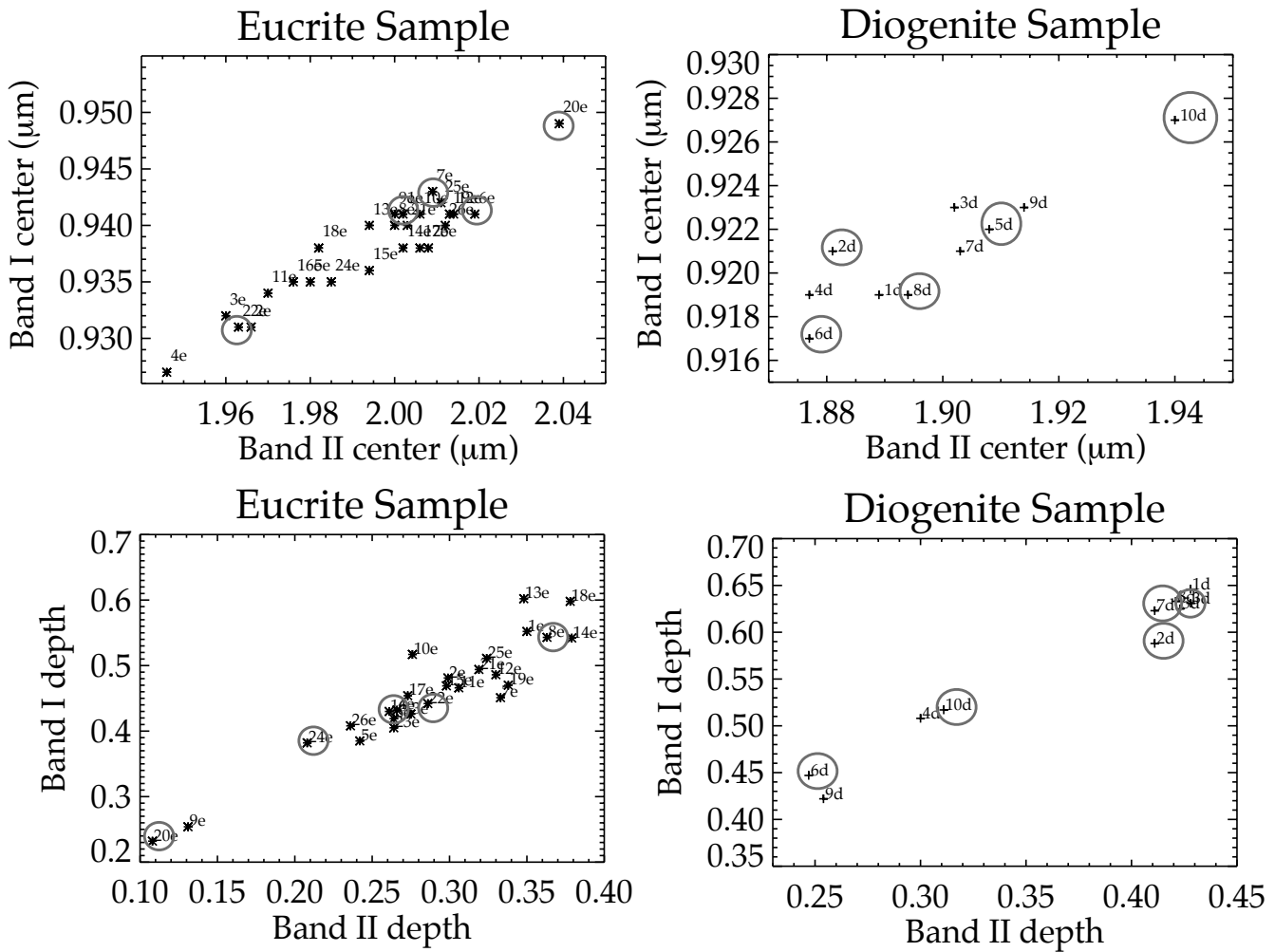


Figure 2

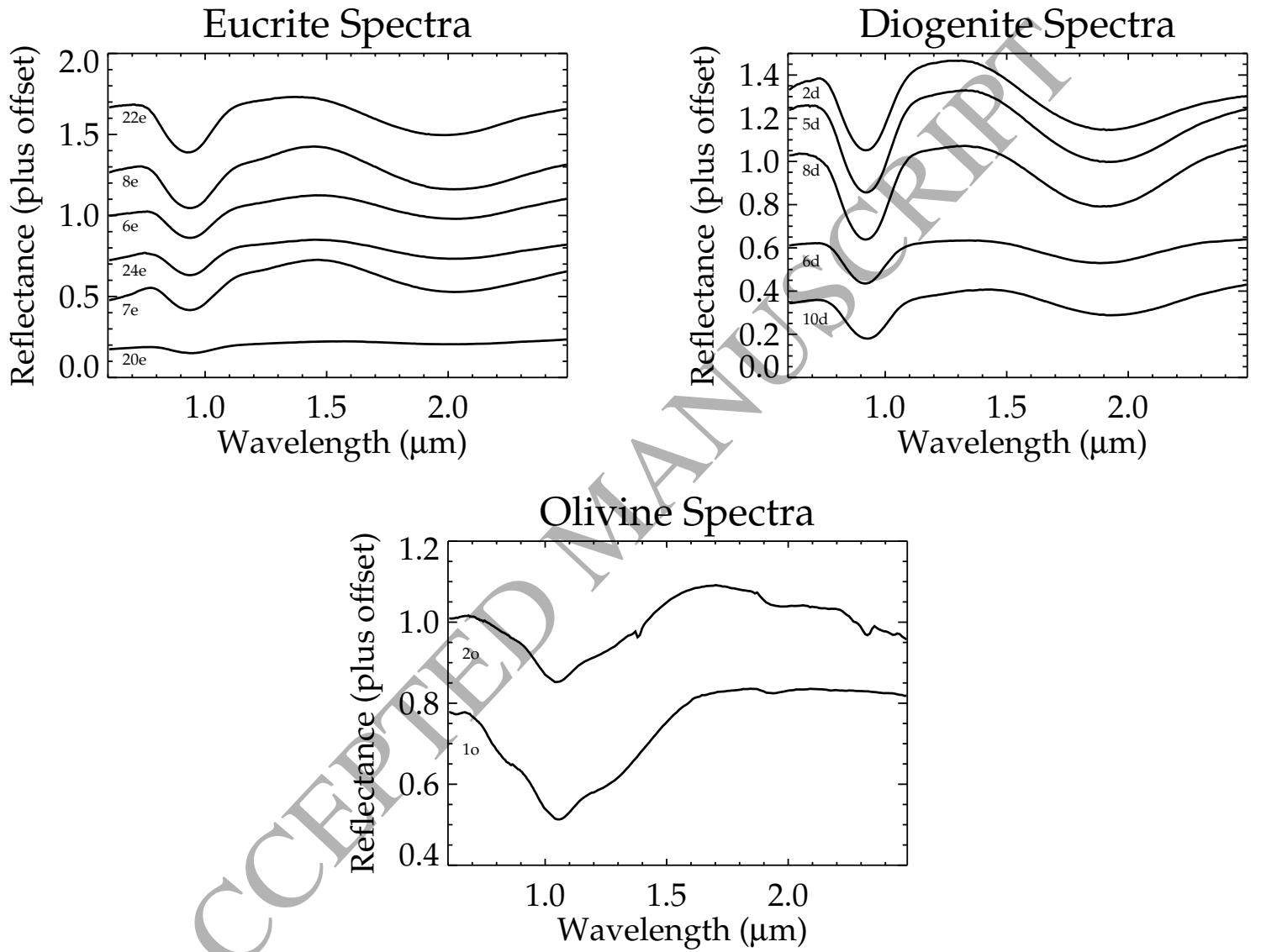


Figure 3

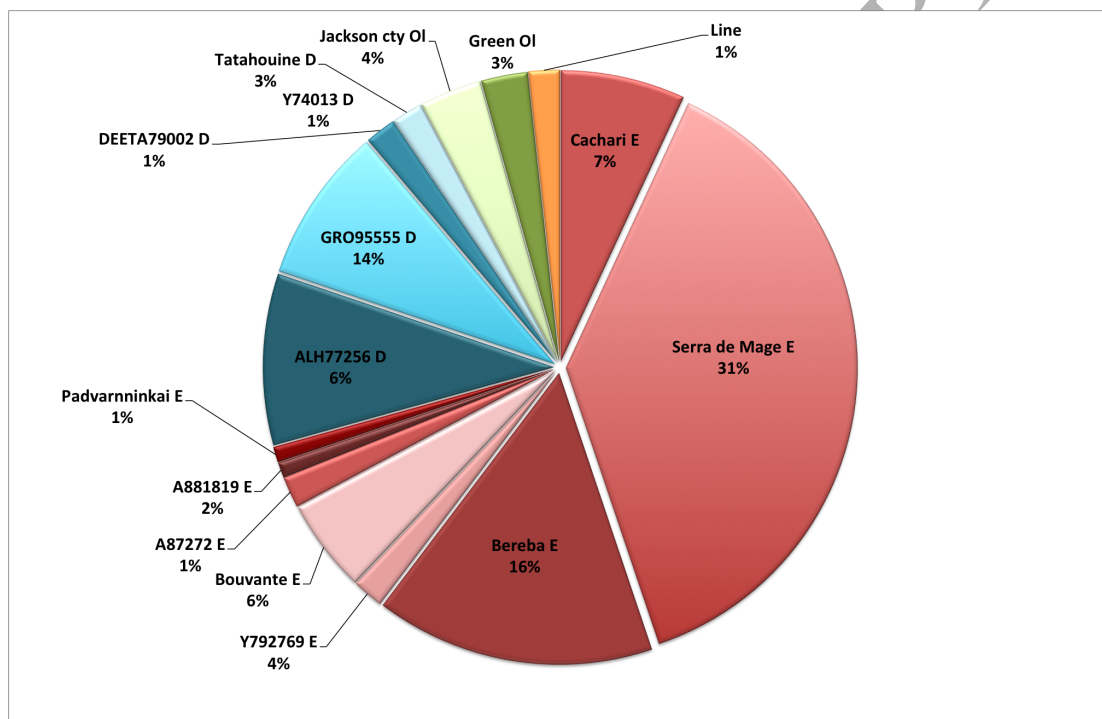


Figure 4

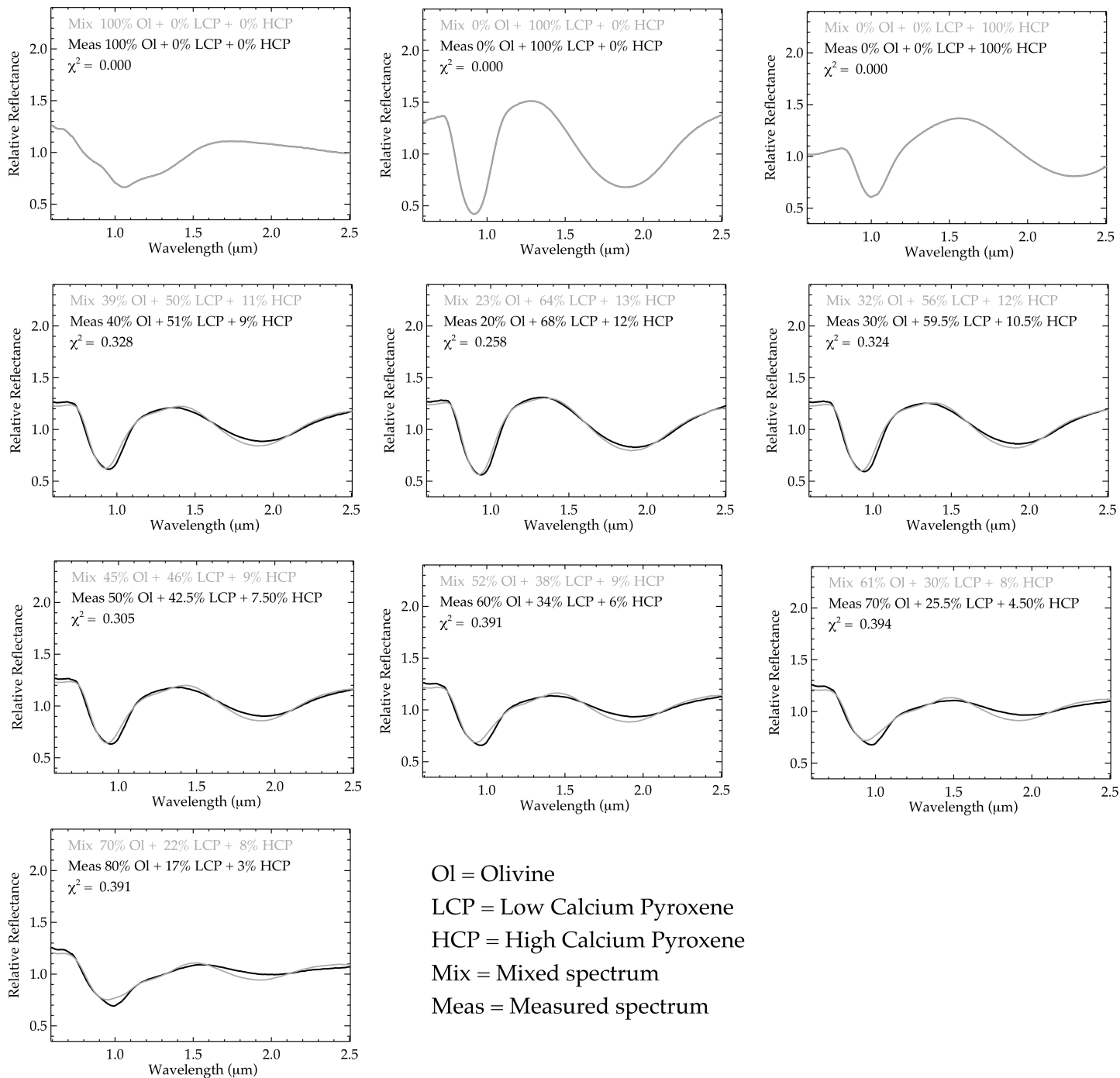


Figure 5

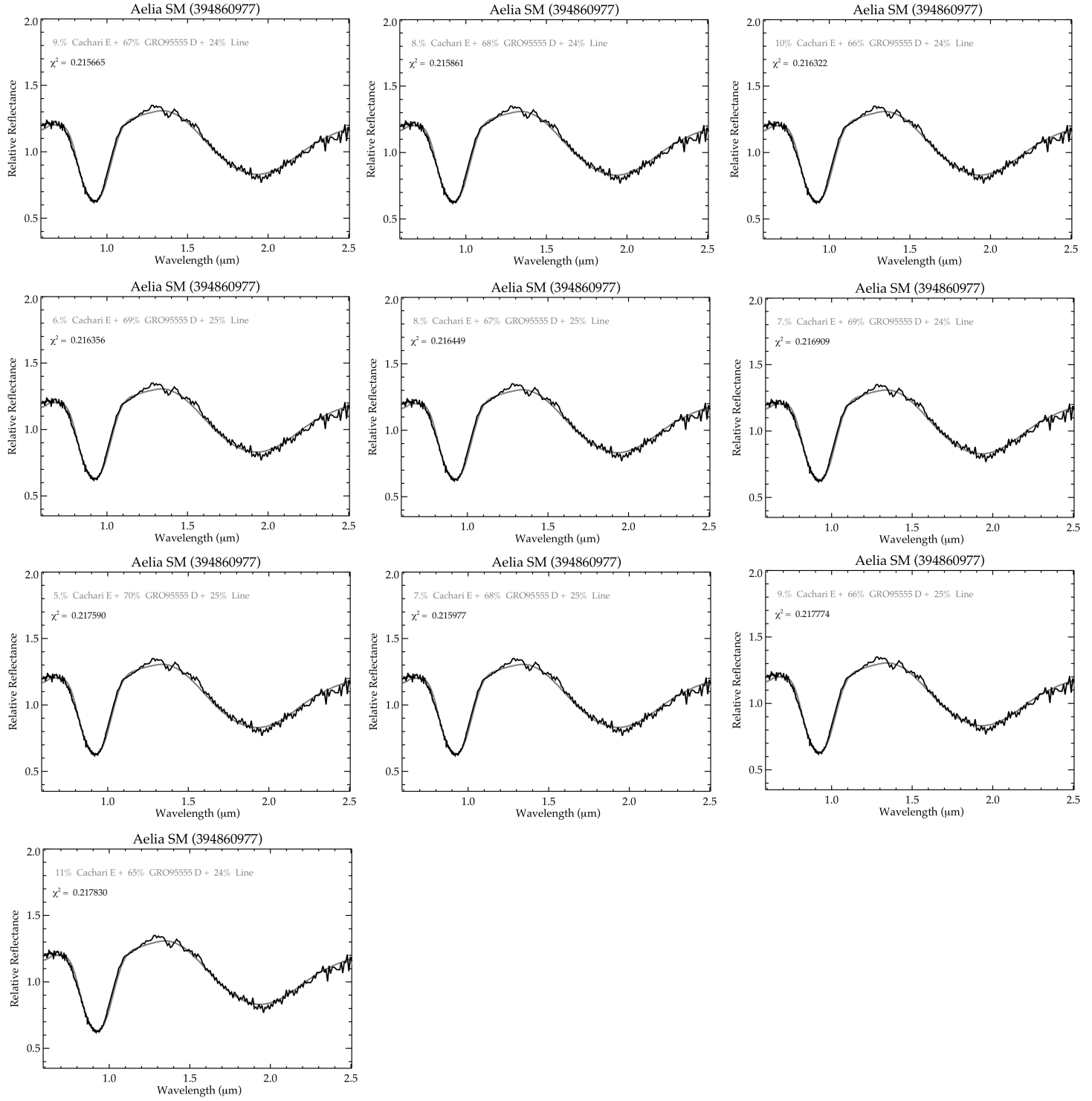


Figure 6

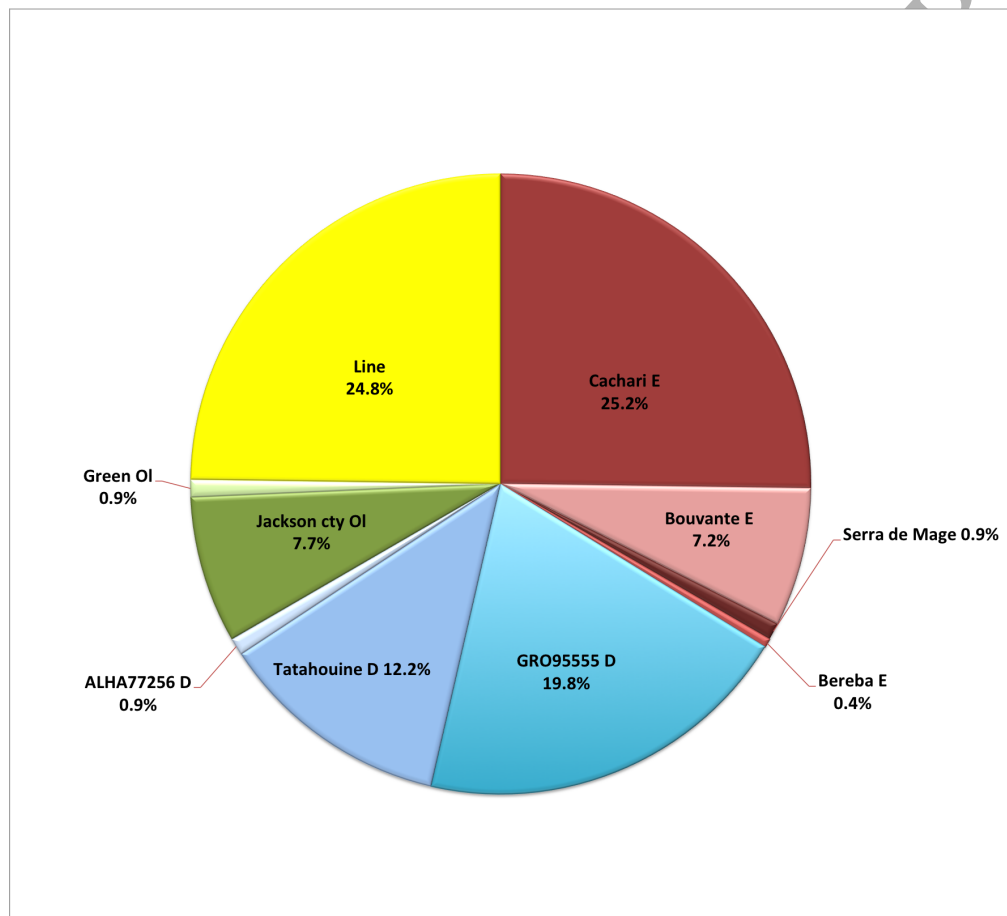


Figure 7

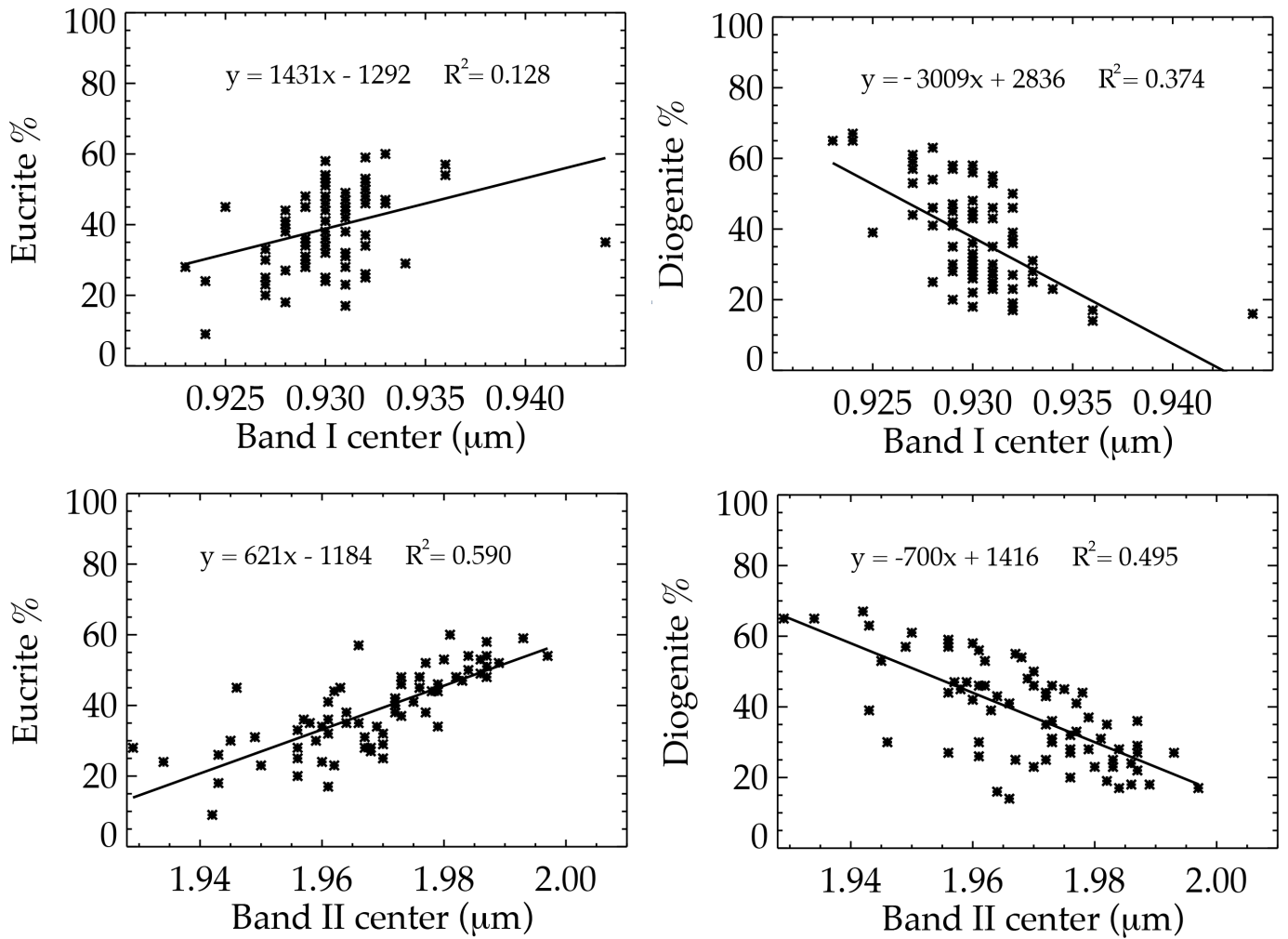


Figure 8

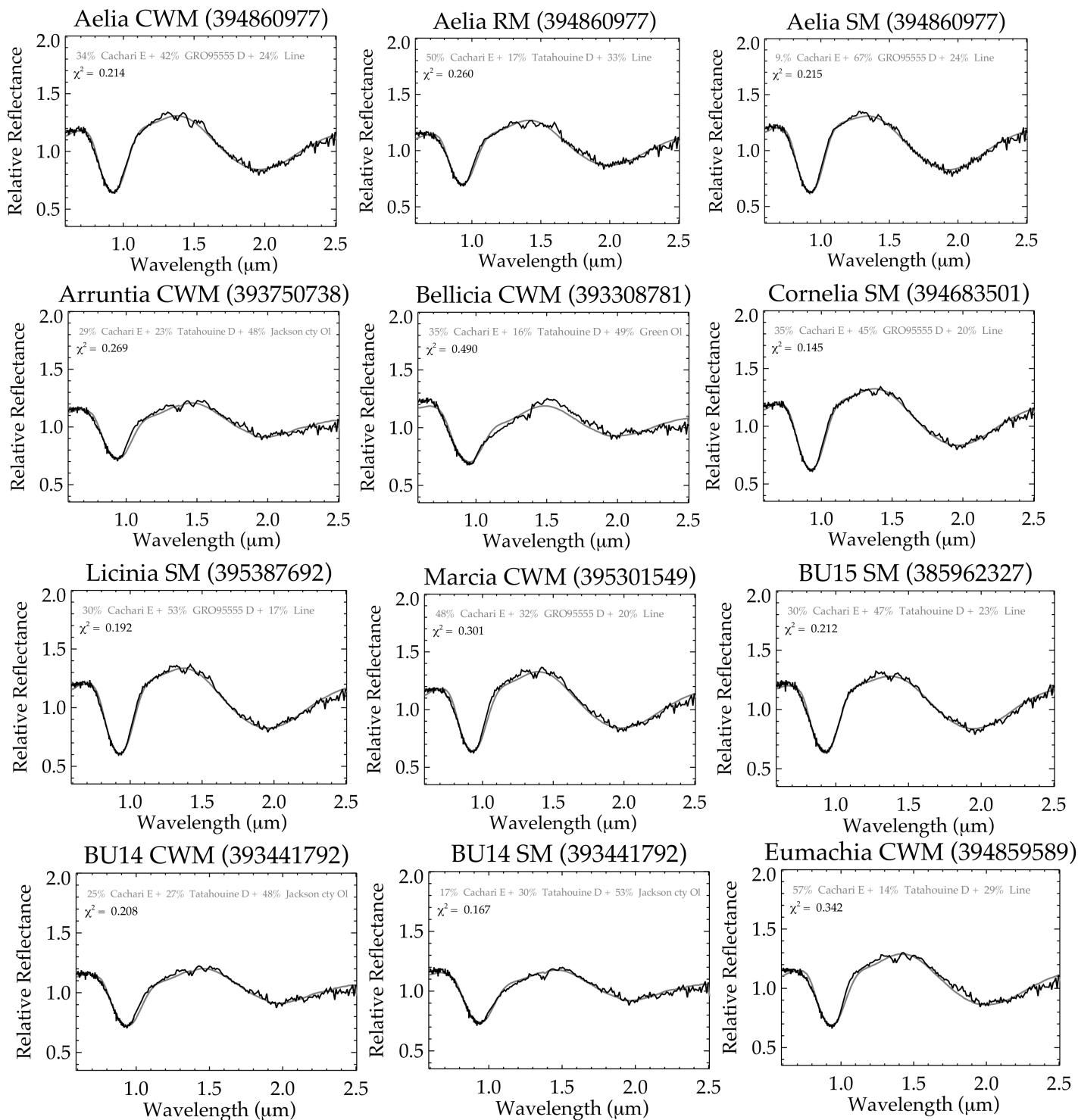


Figure 9

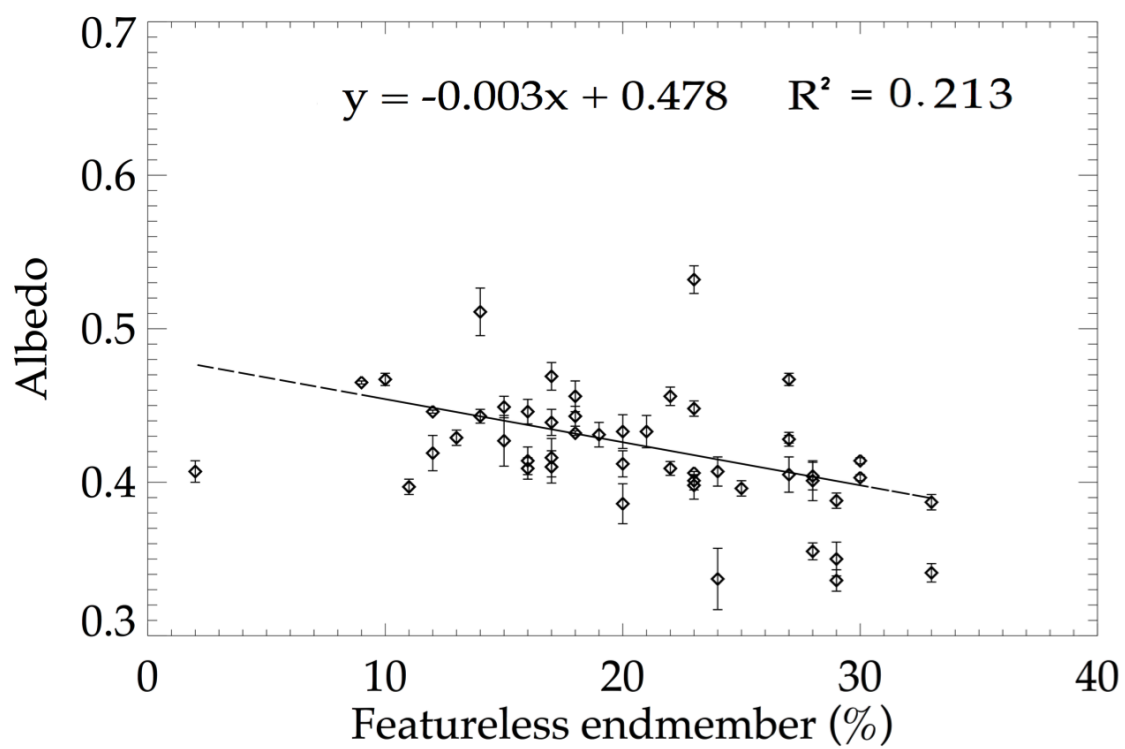


Figure 10

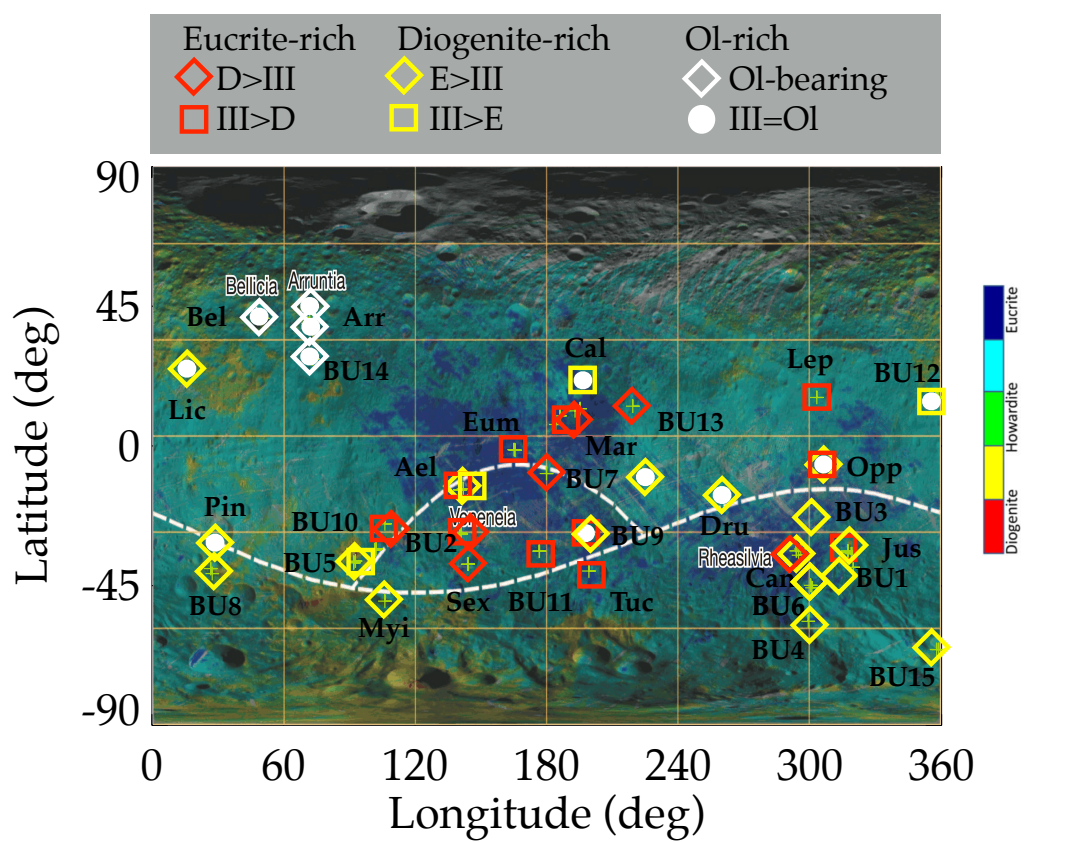


Figure 11

Endmembers						
#	name	type	BCI	BCII	BDI	BDII
1e	A-87272	Eucrite-mmict	0.941	2.002	0.552	0.350
2e	A-881819	Eucrite	0.931	1.966	0.481	0.299
3e	ALH78132	Eucrite-pmict	0.932	1.960	0.426	0.275
4e	ALH85001	Eucrite-Mg rich	0.927	1.946	0.432	0.266
5e	ALHA76005	Eucrite-pmict	0.935	1.980	0.385	0.242
6e	<u>Bereba</u>	Eucrite-mmict	0.941	2.019	0.419	0.264
7e	<u>Bouvante</u>	Eucrite-mmict	0.945	2.009	0.451	0.333
8e	<u>Cachari</u>	Eucrite-mmict	0.940	2.000	0.543	0.363
9e	EET 87542	Eucrite-br	0.941	2.000	0.254	0.131
10e	EET 90020	Eucrite-unbr	0.941	2.006	0.517	0.276
11e	EETA79005	Eucrite-pmict	0.934	1.970	0.466	0.306
12e	GRO 95533	Eucrite-br	0.941	2.014	0.486	0.330
13e	Ibitira	Eucrite-mmict	0.940	1.994	0.602	0.348
14e	Jonzac	Eucrite-mmict	0.938	2.002	0.542	0.379
15e	Juvinas	Eucrite-mmict	0.936	1.994	0.469	0.298
16e	LEW 87004	Eucrite-pmict	0.935	1.976	0.430	0.261
17e	Millbillillie	Eucrite-mmict	0.938	2.006	0.454	0.273
18e	Moore County	Eucrite-cm	0.938	1.982	0.598	0.378
19e	PCA 82502	Eucrite-unbr	0.941	2.013	0.470	0.338
20e	<u>Padvarninkai</u>	Eucrite-mmict	0.949	2.039	0.232	0.108
21e	Pasamonte	Eucrite-pmict	0.940	2.003	0.494	0.319
22e	<u>SerradeMage</u>	Eucrite-cm	0.931	1.963	0.442	0.286
23e	Stannern	Eucrite-mmict	0.938	2.008	0.405	0.264
24e	<u>Y74450</u>	Eucrite-pmict	0.935	1.985	0.382	0.208
25e	Y792510	Eucrite-mmict	0.942	2.011	0.511	0.324
26e	Y792769	Eucrite-pmict	0.940	2.012	0.408	0.236
1d	A881526	Diogenite	0.919	1.889	0.646	0.428
2d	<u>ALH77256</u>	Diogenite	0.921	1.881	0.588	0.411
3d	Aioun el Atrouss	Diogenite-pm	0.923	1.902	0.631	0.428
4d	EETA79002	Diogenite	0.919	1.877	0.508	0.300
5d	<u>GRO95555</u>	Diogenite-an	0.922	1.908	0.625	0.428
6d	<u>Johnstown</u>	Diogenite	0.917	1.877	0.447	0.247
7d	LAP 91900	Diogenite	0.921	1.903	0.623	0.411
8d	<u>Tatahouine</u>	Diogenite	0.919	1.894	0.633	0.421
9d	Y74013	Diogenite	0.923	1.914	0.422	0.254
10d	<u>Y75032</u>	Diogenite	0.927	1.940	0.517	0.311
1o	<u>Jackson cty</u>	Olivine	1.056	-	0.361	-
2o	<u>Green olivine</u>	Olivine	1.054	-	0.226	-

Table 1

Linear unmixing results applied to the BM units

BM unit	Cube	Endm 1	Abundance	Endm 2	Abundance	Endm 3	Abundance	χ^2	r
BU1 RM	(372521396)	Cachari E	0.28	GRO95555 D	0.52	Line	0.20	0.201	0.994
BU2 CWM	(372741836)	Cachari E	0.46	GRO95555 D	0.28	Line	0.26	0.447	0.982
BU2 SM	(372741836)	Cachari E	0.47	Tatahouine D	0.25	Line	0.28	0.342	0.986
BU2 CWM	(395611823)	SerradeMage E	0.86	Jackson cty Ol	0.12	Line	0.02	0.204	0.989
BU2 SM	(395611823)	Cachari E	0.47	Tatahouine D	0.23	Line	0.30	0.247	0.989
BU3 RM	(372385964)	Cachari E	0.32	GRO95555 D	0.46	Line	0.22	0.342	0.989
BU4 CWM	(372212906)	Cachari E	0.41	GRO95555 D	0.45	Line	0.14	0.472	0.987
BU5 CWM	(371993041)	Bouvante E	0.28	GRO95555 D	0.65	Line	0.07	0.705	0.989
BU5 RM	(371993041)	Cachari E	0.20	GRO95555 D	0.57	Line	0.23	0.306	0.990
BU5 SM	(371993041)	Cachari E	0.33	GRO95555 D	0.44	Line	0.23	0.386	0.987
BU6 RM	(372078317)	Cachari E	0.34	GRO95555 D	0.48	Line	0.18	0.312	0.970
BU6 SM	(372078317)	Cachari E	0.44	GRO95555 D	0.44	Line	0.12	0.302	0.992
BU7 RM	(394993455)	Cachari E	0.52	GRO95555 D	0.33	Line	0.15	0.281	0.992
BU8 CWM	(394155284)	Bouvante E	0.24	GRO95555 D	0.65	Line	0.11	0.351	0.991
BU8 SM	(394155284)	Bouvante E	0.23	GRO95555 D	0.61	Line	0.16	0.278	0.977
BU9 CWM	(372430301)	Bouvante E	0.34	Tatahouine D	0.37	Jackson cty Ol	0.29	0.242	0.989
BU9 RM	(372430301)	Cachari E	0.48	Tatahouine D	0.19	Line	0.33	0.229	0.989
BU10 CWM	(371992493)	Cachari E	0.45	GRO95555 D	0.28	Line	0.27	0.296	0.985
BU10 SM	(371992493)	Cachari E	0.51	Tatahouine D	0.22	Line	0.27	0.271	0.988
BU10 CWM	(372609208)	Cachari E	0.44	GRO95555 D	0.28	Line	0.28	0.362	0.973
BU10 SM	(372609208)	Cachari E	0.49	Tatahouine D	0.24	Line	0.27	0.233	0.990
BU11 CWM	(371815732)	Cachari E	0.48	Tatahouine D	0.20	Line	0.32	0.214	0.990
BU11 SM	(372874554)	Cachari E	0.52	Tatahouine D	0.18	Line	0.30	0.280	0.987
BU11 SM	(393801089)	Cachari E	0.53	Tatahouine D	0.18	Line	0.29	0.341	0.985
BU12 CWM	(371632826)	Bouvante E	0.25	GRO95555 D	0.50	Jackson cty Ol	0.25	0.530	0.980
BU12 SM	(371632826)	Bouvante E	0.23	GRO95555 D	0.53	Jackson cty Ol	0.24	0.501	0.982
BU13 SM	(371986649)	Cachari E	0.46	GRO95555 D	0.36	Line	0.18	0.333	0.989
BU14 CWM	(393441792)	Cachari E	0.25	Tatahouine D	0.27	Jackson cty Ol	0.48	0.208	0.988
BU14 SM	(393441792)	Cachari E	0.17	Tatahouine D	0.30	Jackson cty Ol	0.53	0.167	0.989
BU15 CWM	(385962327)	Cachari E	0.32	Tatahouine D	0.56	Line	0.12	0.421	0.989
BU15 SM	(385962327)	Cachari E	0.30	Tatahouine D	0.47	Line	0.23	0.212	0.993

continue

Linear unmixing results applied to the BM units									
BM unit	Cube	Endm 1	Abundance	Endm 2	Abundance	Endm 3	Abundance	χ^2	r
Arruntia CWM	(393750738)	Cachari E	0.29	Tatahouine D	0.23	Jackson cty Ol	0.48	0.269	0.984
Arruntia RM	(393750391)	Bereba E	0.36	Tatahouine D	0.26	Jackson cty Ol	0.38	0.194	0.966
Arruntia SM	(393750738)	Cachari E	0.31	GRO95555 D	0.25	Green Ol	0.44	0.264	0.988
Aelia CWM	(394860977)	Cachari E	0.34	GRO95555 D	0.42	Line	0.24	0.214	0.992
Aelia RM	(394860977)	Cachari E	0.50	Tatahouine D	0.17	Line	0.33	0.260	0.987
Aelia SM	(394860977)	Cachari E	0.09	GRO95555 D	0.67	Line	0.24	0.215	0.993
Bellicia CWM	(393308781)	Cachari E	0.35	Tatahouine D	0.16	Green Ol	0.49	0.490	0.981
Calpurnia CWM	(395166561)	Bouvante E	0.26	Tatahouine D	0.39	Jackson cty Ol	0.35	0.270	0.987
Canuleia CWM	(394198821)	Cachari E	0.45	Tatahouine D	0.39	Line	0.16	0.459	0.983
Canuleia RM	(394198821)	Cachari E	0.44	GRO95555 D	0.46	Line	0.10	0.539	0.987
Canuleia SM	(394198821)	Bouvante E	0.28	Serra de Mage E	0.25	GRO95555 D	0.47	0.632	0.984
Canuleia RM	(394198127)	Cachari E	0.35	GRO95555 D	0.41	Line	0.24	0.353	0.988
Canuleia RM	(371905283)	Cachari E	0.60	GRO95555 D	0.31	Line	0.09	0.577	0.985
Cornelia CWM	(371813008)	Bouvante E	0.28	GRO95555 D	0.58	Jackson cty Ol	0.14	0.381	0.989
Cornelia CWM	(394683501)	Cachari E	0.36	GRO95555 D	0.47	Line	0.17	0.157	0.995
Cornelia SM	(394683501)	Cachari E	0.35	GRO95555 D	0.45	Line	0.20	0.145	0.995
Cornelia CWM	(373313780)	Bouvante E	0.31	GRO95555 D	0.57	Jackson cty Ol	0.12	0.485	0.986
Cornelia SM	(373313780)	Bouvante E	0.25	GRO95555 D	0.59	Jackson cty Ol	0.16	0.315	0.991
Drusilla CWM	(393931377)	Bouvante E	0.28	GRO95555 D	0.55	Jackson cty Ol	0.17	0.420	0.987
Drusilla SM	(393931377)	Bouvante E	0.37	Tatahouine D	0.46	Jackson cty Ol	0.17	0.368	0.987
Eumachia CWM	(394859589)	Cachari E	0.57	Tatahouine D	0.14	Line	0.29	0.342	0.985
Eumachia SM	(394859589)	Cachari E	0.54	Tatahouine D	0.17	Line	0.29	0.328	0.985
Justina CWM	(372520864)	Cachari E	0.54	Tatahouine D	0.28	Line	0.18	0.296	0.991
Justina RM	(372520864)	Cachari E	0.38	GRO95555 D	0.43	Line	0.19	0.264	0.989
Justina SM	(372520864)	Cachari E	0.42	GRO95555 D	0.35	Line	0.23	0.305	0.989
Justina CWM	(371904187)	Cachari E	0.58	Tatahouine D	0.27	Line	0.15	0.370	0.983
Justina RM	(371904187)	Cachari E	0.41	GRO95555 D	0.44	Line	0.15	0.323	0.992
Justina SM	(371904187)	Cachari E	0.54	Tatahouine D	0.29	Line	0.17	0.335	0.989
Lepida SM	(395256929)	Cachari E	0.45	ALHA77256 D	0.30	Line	0.25	0.595	0.977
Licina CWM	(395387692)	Bouvante E	0.18	GRO95555 D	0.63	Jackson cty Ol	0.19	0.273	0.992
Licina SM	(395387692)	Cachari E	0.30	GRO95555 D	0.53	Line	0.17	0.192	0.994
Marcia CWM	(395301166)	Cachari E	0.53	GRO95555 D	0.23	Line	0.24	0.410	0.984
Marcia SM	(395301166)	Cachari E	0.46	GRO95555 D	0.31	Line	0.23	0.396	0.986
Marcia CWM	(395301549)	Cachari E	0.48	GRO95555 D	0.32	Line	0.20	0.301	0.990
Marcia SM	(395301549)	Cachari E	0.48	GRO95555 D	0.30	Line	0.22	0.353	0.987
Myia RM	(372300571)	Cachari E	0.38	GRO95555 D	0.41	Line	0.21	0.396	0.987
Oppia CWM	(373136361)	Bouvante E	0.38	Tatahouine D	0.43	Jackson cty Ol	0.19	0.364	0.986
Oppia SM	(373136361)	Cachari E	0.45	GRO95555 D	0.27	Line	0.28	0.309	0.979
Pinaria CWM	(371727131)	Cachari E	0.41	ALHA77256 D	0.46	Line	0.13	0.332	0.990
Pinaria SM	(371727131)	Bouvante E	0.27	GRO95555 D	0.54	Jackson cty Ol	0.19	0.308	0.990
Sextilia CWM	(371816828)	Cachari E	0.48	GRO95555 D	0.35	Line	0.17	0.461	0.986
Sextilia SM	(371816828)	Cachari E	0.48	GRO95555 D	0.36	Line	0.16	0.484	0.986
Tuccia RM	(372565807)	Cachari E	0.59	Tatahouine D	0.27	Line	0.14	0.319	0.990

Table 2